Cement and Concrete Composites 134 (2022) 104766

Contents lists available at ScienceDirect

Cement and Concrete Composites

journal homepage: www.elsevier.com/locate/cemconcomp

Role of biopolymers in enhancing multiscale characteristics of carbonation-cured cementitious composites

Rakibul I. Khan [a,c], Muhammad Intesarul Haque [a], Warda Ashraf [a,*], Surendra Shah [a], Navid Saleh [b]

[a] Department of Civil Engineering, University of Texas at Arlington, Nedderman Hall, Arlington, TX, 76010, USA
[b] Civil, Architectural and Environmental Engineering, University of Texas at Austin, Austin, TX, 78712, USA
[c] Laticrete International, Inc., Bethany, CT, 06524-3423, USA

ARTICLE INFO

Keywords:
Polydopamine
Nanocellulose
Carbonation
Slag
Calcium carbonate
CO_2 footprint
OPC

ABSTRACT

This study investigates the application of two natural biopolymers, i.e., polydopamine and nanocellulose, as performance-enhancing additives in carbonation-cured ordinary Portland cement (OPC) - slag blended composites. A multiscale investigation reveals that the addition of these biopolymers increases the formation of nanoporosity and reduces amounts of microporosity in the matrixes. Both biopolymers are also found to increase the degree of reaction in the binders. Incorporation of 0.05 wt% polydopamine increases the flexural strength of the composites by 55% after 28 days of curing. A similar flexural strength improvement (~66%) can also be achieved by adding nanocellulose. Moreover, the addition of these biopolymers increases the early age (~3 days) compressive strength of the carbonated composites by nearly 35%. It is postulated that the addition of polydopamine enhances performance by creating stronger bonds with the reaction products and by stabilizing amorphous $CaCO_3$. On the other hand, the addition of nanocellulose improves the strength by bridging microcracks.

1. Introduction

The cement and concrete industry accounts for 9% of the global anthropogenic CO_2 emissions [1,2]. Using alternative cementitious materials rather than ordinary Portland cement (OPC) can facilitate minimizing the CO_2 footprint of the concrete industry. Ground granulated blast furnace slag (commonly known as 'GGBFS' or slag) is one of the most well-known alternative cementitious materials with a significantly lower carbon footprint. Slag is a by-product produced during the manufacturing of steel. For every tonne of steel produced, approximately 30 kg of ladle slag is produced [3]. Slag-based cement composites are cheaper, environment friendly, and have also demonstrated greater durability, as evidenced by their resistance to chemicals and chloride penetration [4–7]. When used as a partial replacement for OPC in concrete production, slag reacts slowly and gains strength through pozzolanic activity over time [8]. However, slag can also be activated by carbonation curing, resulting in enhanced early strength [3,7]. Previous studies have demonstrated that such carbonation-cured composites may store up to 18% of CO_2 by weight, making this an attractive method for CO_2 sequestration [9,10].

During carbonation-curing, calcium silicate (or calcium aluminosilicate) in Ca-rich binders reacts with CO_2 in the presence of water to produce $CaCO_3$ and Ca-modified silica gel [11], which are the primary binding phases in this matrix. In addition to the degree of reaction, the polymorphs of $CaCO_3$ control the mechanical performance of the carbonation-cured calcium silicate cementitious composites [11]. Primarily, four different $CaCO_3$ polymorphs can be present in carbonation-cured composites, including calcite, vaterite, aragonite, and amorphous $CaCO_3$ (ACC). The formation of $CaCO_3$ polymorphs follows the Ostwald's process, which begins with the formation of amorphous $CaCO_3$, followed by the formation of more stable polymorphs, such as aragonite, vaterite, and finally, calcite [11–14].

A variety of bio-additives can be used to control the formation of these polymorphs [15–17]. A few studies in cementitious composites have used different inorganic materials to regulate the formation of polymorphs and investigated their effects on mechanical performance [11,18,19]. It is important to note that $CaCO_3$ is also the most abundant biomineral, occurring naturally in algae, mussel shells, and sea urchin

* Corresponding author.
E-mail address: warda.ashraf@uta.edu (W. Ashraf).

https://doi.org/10.1016/j.cemconcomp.2022.104766
Received 13 January 2022; Received in revised form 19 July 2022; Accepted 10 September 2022
Available online 21 September 2022
0958-9465/© 2022 Elsevier Ltd. All rights reserved.

Table 1
Composition of OPC and slag.

	SiO_2	CaO	Al_2O_3	Fe_2O_3	MgO	SO_3	MnO
OPC (weight %)	21.2	65.3	3.87	3.10	0.82	4.28	0.20
Slag (weight %)	29.6	36.4	15.6	0.37	9.69	5.19	0.49

spines [20]. There are also abundant biopolymers that can control $CaCO_3$ crystallization [17,21–25].

Accordingly, the literature is rich in studies evaluating the role of organic biomolecules on the in-situ crystallization of $CaCO_3$ [15,23,26–31]. Inspired by these studies, Khan et al. achieved success in controlling the polymorphs of $CaCO_3$ in carbonation-cured wollastonite systems using amino acids [11]. However, natural amino acids are expensive, which may limit their application in the cement and concrete industry. In addition to amino acids, previous reports identify that certain abundant biopolymers, including polydopamine (PDA) [17,21–23] and cellulose nanofibers (CNFs) [16,32], can also control $CaCO_3$ crystallization in the case of biomineralization. However, the roles of these abundant biopolymers in carbonation-cured hydraulic/semi-hydraulic cementitious materials remain unknown.

Polydopamine (PDA) is well-known for its adhesive properties. Mussels release adhesive proteins that are primarily composed of dihydroxy-L-phenylalanine (DOPA) and lysine, which extensively polymerize under wet alkaline conditions. Dopamine hydrochloride contains the same catechol functional group as the side chain of DOPA residues and the same amine functional group as lysine, making it an excellent adhesive for a wide variety of inorganic and organic materials, because of its self-polymerization ability to form PDA [22]. PDA is often utilized as a crystal modifier [17,20,23] and as a coating additive due to its adhesive properties [19]. Saleh et al. utilized dopamine hydrochloride in a hydraulic OPC and investigated its influence on the hydration system [33], whereas Fang et al. applied PDA in fine sand to improve its adherence to cement particles [18]. The effects of PDA in CO_2 -cured cementitious composites remains unexplored.

On the other hand, cellulose is the most abundant naturally occurring organic biopolymer with a wide range of applications [34]. It can be derived from bacteria, algae, and sea creatures [35]. It consists of polysaccharides; i.e., D-glucose and 1,4-glycosides [34,36,37]. Its renewability, natural abundance and low cost, as well as inherent mechanical strength set it apart from other biopolymers [34,38]. The use of CNFs in cement-based composites is being investigated because of its long molecular chains [36,37] and high aspect ratio (width: 4–20 nm, length: 500–2000 nm) [39] that give rise to reinforcing abilities [24,25], yield higher Young's Modulus (65-110 GPA) [40], and thermal stability [41]. Additionally, cellulosic nanomaterials have been used with amorphous $CaCO_3$ to produce composite materials with superior properties [42]. Although CNFs have been used in hydration-based cementitious materials [43], application of these biopolymers in carbonation-based composites have not been studied yet.

This study addresses the aforementioned knowledge gaps and focuses on the applications of PDA and CNFs to control $CaCO_3$ polymorph formation in a cementitious environment and evaluates the effectiveness of these biopolymers as performance-enhancing additives for CO_2-cured cementitious composites. The specific research objectives of this study are: (i) to investigate the effects of biopolymers on the macroscale performance (i.e., shrinkage, compressive strength, flexural strength) of CO_2-cured calcium silicate composites, (ii) to understand how the presence of PDA and CNF affects the formation of carbonate phases, and (iii) to investigate the effects of selected biopolymers on the nano-to micro-structural formations in CO_2-cured calcium silicate composites.

2. Materials and methods

2.1. Materials

Mortar samples were prepared using OPC (type I/II), GGBFS slag (Cemex, Texas, USA), and ASTM standard sand. Table 1 summarizes the chemical compositions of the OPC and slag. The CNF was extracted from bleached hardwood pulp and was supplied by Cellulose Lab (Canada). CNF was supplied as a slurry, containing 1 wt% concentration of fibers in water. The average width and length of the fibers were around 10–60 nm and 800–3000 nm, respectively. Dopamine hydrochloride ($C_{18}H_{11}NO_2$–HCl) was purchased from VWR International (Pennsylvania, USA). Due to the alkaline cementitious environment, dopamine hydrochloride ($C_{18}H_{11}NO_2$–HCl) self-polymerizes to form PDA, when added to the paste mixture. From here-on, the samples produced with dopamine hydrochloride ($C_{18}H_{11}NO_2$–HCl) are address as the PDA-containing batches.

2.2. General mixture proportion, sample preparation, and curing conditions

For preparing the paste and mortar samples, 1:1 OPC: slag was mixed with a constant water to a binder ratio of 0.40. Based on the CNF and PDA content, three distinct batches of paste samples were prepared for mechanical and microstructural investigation. In the first batch, 0.05, 0.1, and 0.3 (wt.%) CNF were added to the binder mixture. In the second batch, 0.05, 0.10, and 0.30 (wt.%) PDA were added to the paste mixture. In the third batch, the paste combination contained 0.05, 0.1, and 0.3 (wt.%) of CNF and PDA (50% CNF and 50% PDA). The batch that did not contain any biopolymer is referred to as the 'control' batch. Details of the samples' mix design are shown in Table 2. These doses were determined based on earlier research that showed that a low dose of biopolymer effectively improves the performance of cementitious composites [18,33,44–47].

The following procedures were used for mixing pastes: (i) for homogenization, CNF slurry/PDA was mixed with water for 2 min, (ii) dry binder (50% OPC with 50% slag) was added to this suspension and mixed for 2 min at 140 rpm, (iii) after 30 s of rest (during this time

Table 2
Paste sample mix design based on 1000 g of binder with a w/b ratio of 0.40

Biopolymers	Doses (binder wt.%)	Binder[a] (g)	(PDA)[b] (g)	CNF slurry (g)	Free water (g)	Total water (g)
Control	0.00%	1000	0.00	0	400	400
Polydopamine (PDA)	0.05%	1000	0.50	0	400	400
	0.10%	1000	1.00	0	400	400
	0.30%	1000	3.00	0	400	400
CNF	0.05%	1000	0.00	50	350.5	400
	0.10%	1000	0.00	100	301	400
	0.30%	1000	0.00	300	103	400
CNF-Polydopamine (PDA)	0.05%	1000	0.25	25	375.25	400
	0.10%	1000	0.50	50	350.5	400
	0.30%	1000	1.50	150	251.5	400

[a] Binder contains 50% OPC and 50% slag (i.e., 500g OPC and 500g slag in 1000g binder).
[b] PDA was added in form of dopamine hydrochloride ($C_{18}H_{11}NO_2$–HCl).

scraped down into the batch any paste that may have collected on sides of the bowl), the mixture was again mixed for 1 min at 285 rpm, (iv) the paste mixture was used to cast 25 mm × 25 mm cubes and 40 mm × 20 mm × 15 mm beams in two layers on a vibrator table. Immediately following the casting of the beams and cubes, the samples were placed in a moist curing room at 25 °C and 80% relative humidity (RH). After 24 h, the beams and cubes were demolded and placed in a carbonation chamber with a 20% CO_2 concentration, 80% RH, and at 50 °C until the day of testing. The flexural and compressive strengths of the beam and cube samples were determined after 3, 7, 14, and 28 days of curing from the date of casting. The tested samples were immersed in isopropanol for 24 h to allow for solvent exchange, prior to drying in a vacuum desiccator. These dried samples were used for additional microstructural investigation as described in section 2.3.

Mortar samples were used to monitor the length change, following ASTM C 157 standard [48]. CNF/PDA was first homogenized in water for 2 min, prior to using it in mortar samples. Following that, OPC and slag were mixed with the suspension for 2 min at 140 rpm maintaining, the water to binder ratio as 0.40. After the initial 30 s of mixing, ASTM standard sand was added for 30 s, and the mixing was continued for another minute. Following a 30 s pause to scrape down into the batch any mortar that may have collected on the side of the bowl, the mixer was again set in motion for 1 min at 285 rpm. The mixed mortar samples were used to cast 25 mm × 25 mm × 285 mm prisms. Those prisms were prepared in three layers per the standard. The prisms were immediately placed inside the above-mentioned moist room after casting. After 24 h, the prisms were demolded and placed in the previously stated carbonation chamber, where length variations were observed for up to 56 d.

2.3. Test methods

2.3.1. Mechanical performances

The compressive and flexural strength of the 25 mm × 25 mm cube and 40 mm × 20 mm × 15 mm beam paste samples were measured after 3, 7, 14, and 28 d of carbonation curing. At least three samples were tested in each case, and the average values were reported. The compressive strength was measured via MTS Landmark servo hydraulic test system at a displacement rate of 0.02 mm/s. The flexural strength was measured with MTS Criterion Model 43 at a displacement rate of 0.2 mm/min.

2.3.2. Length change

The length change was measured with the mortar samples indicated in the sample preparation section; prepared in accordance with the ASTM C157 standard [48]. Length was calculated with the following equation (eqn. (1)) in accordance with ASTM C157,

$$Length\ chnage\ (\%) = \frac{CRD_f - CRD_i}{250} \times 100 \quad (1)$$

Here, CRD = difference between the comparator reading of the specimen and the reference bar at any age; *f* and *i* subscripts denote final and initial CRD values, respectively.

2.3.3. Thermogravimetric analysis

A commercially available thermogravimetric analyzer (TGA 550, TA instruments, Delaware, USA) was used for the paste samples. The collected samples were ground with a mortar pestle to obtain a fine powder. Approximately 30–40 mg of #200 sieve-passing powdered sample was loaded into a platinum pan and kept in isothermal condition for 5 min at 25 °C. Temperature of the chamber was then raised to 980 °C with an increment of 15 °C per min. Nitrogen gas was purged to ensure an inert environment. Initially, for a few batches, three replicates were tested with TGA to validate for any deviation in carbonation across samples. The test result deviations were less than 2 wt% of the total carbonated samples. Due to low deviation, TGA was performed with only one sample for the remaining batches.

2.3.4. Fourier transformed infrared (FTIR) spectra

Powdered samples were used for FTIR measurements. A commercially available Nicolet iS50 FTIR from Thermo Scientific (Massachusetts, USA) was used for this test. Spectra were collected using the Attenuated Total Reflection (ATR) mode with 4 cm^{-1} resolution and 32 scans per sample.

2.3.5. X-ray diffraction (XRD)

X-ray diffraction patterns of the paste samples were collected with a Bruker D-500 spectrometer using Cu Kα radiation (40 kV, 30 mA). Diffraction patterns were obtained for the 2θ range of 5°–60° with a step size of 0.02 (2θ) per second.

XRD spectral analysis was performed using a commercially available software (Match! Phase Analysis using Powder Diffraction, Germany). The PDF card numbers used were PDF #96-900-0967, PDF #96-901-3802, PDF #96-150-8972, PDF #96-901-6126, PDF #96-901-3566 and PDF #96-900-0113, for calcite, aragonite, vaterite, alite, vaterite, and portlandite, respectively.

2.3.6. Mercury intrusion porosimetry (MIP)

Mercury intrusion porosimetry was used to determine the mesoporous (pore radius 2–50 nm) and macro-porous (>50 nm) structures. The MIP test was performed on the control batch and the paste samples containing 0.1% CNF, 0.1% PDA, and 0.1% CNF-PDA dosages after 28 d of carbonation-curing. The sample size was approximately 15 × 15 × 15 mm. MIP experiments were performed on a Micrometrics Instrument Corporation (Norcross, GA) AutoPore IV 9500 V2.03.01 at a maximum pressure of 413 MPa to reach pores with a diameter of 3.02 nm.

2.3.7. Dynamic vapor sorption (DVS)

A commercially available DVS equipment (TA instrument, Q5000) was used to obtain the moisture desorption isotherms of the 28 days cured carbonated paste samples. The desorption isotherms were then analyzed to obtain pore size distribution. Samples were soaked in DI water for 48 h prior to testing to ensure complete saturation. After soaking, approximately 15–20 mg sample was loaded onto a quartz pan. The sample was first equilibrated at 97.5% RH for 96 min; the RH was then gradually reduced (with 5–10% RH gradient) to obtain the desorption isotherm. Mass equilibrium was assumed to have reached (at each RH level) when mass fluctuation was less than 0.001% over 15 min. The experiment was conducted under N_2 purging and at a constant temperature of 23 °C. Compared to MIP or nitrogen sorption, DVS is generally considered to be the preferred technique for characterizing and investigating meso and gel pore structures in cementitious materials, especially those containing CSH or Ca-modified silica gel structures because: (i) water has the smallest molecular size compared to nitrogen or mercury, and thus can access smaller pores; and (ii) as reported by Odler [49], differences in the employed temperature for water and nitrogen adsorption cause water to pass over the energy barrier required for diffusive transport (nitrogen would take several years to equilibrate). As a result, when compared to water sorption, the nitrogen sorption technique significantly underestimates the surface area of cementitious matrixes. In this study, the specific surface area (S_{BET}) of carbonated composites was determined by the BET method [50], and pore size distribution was determined using the BJH model [51]. The calculation of the BET and BJH methods was based on previous studies [52,53].

2.3.8. Scanning electron microscopy (SEM)

The microstructures of the 28-d carbonation-cured samples were evaluated with a Hitachi 3000 N SEM. The instrument was operated at the high vacuum mode with 30 kV accelerated voltage and a working distance of about 10 mm. The cement paste samples were coated with platinum prior to capturing the images.

Fig. 1. OPC-slag cement blended paste samples with the addition of (a) 0.1% CNF, (b) 0.1% PDA, and (c) 0.1% CNF-PDA.

The sample utilized for the nanoindentation experiment (section 2.3.9) was coated with a thin layer of platinum (Pt) after the experiment and was analyzed using SEM with EDS for BSE imaging. The selected images were converted to 32-bit binary images with the same brightness and contrast for ImageJ analysis. Then, in order to achieve a consistent grey value, we set the threshold of the selected images to the same level. Then, using ImageJ's analysis mode, we estimated the area fraction of the dark region.

2.3.9. Nanoindentation

To prepare the samples, a disc of approximately 20 mm diameter and 10 mm thickness was cut with a slow cutting laboratory saw, that was cooled with mineral oil. The detailed procedure to obtain adequate surface finishing for nanoindentation is described elsewhere [54].

For grid nanoindentation (also known as 'statistical nanoindentation [SNI]'), the cement paste samples containing 0.1 wt% CNF, 0.1 wt% PDA and 0.1 wt% CNF and PDA (50% CNF + 50% PDA) were chosen in addition to the control batch samples after 28 d of carbonation-curing. The load function had three segments: (i) loading from zero to maximum in the span of 5 s, (ii) holding at the maximum load for 5 s, (iii) unloading from maximum to zero within 5 s. Selection of the appropriate load function is crucial for obtaining reliable nanoindentation data. The criterion used is that the depth of the indentations should be small enough to determine the mechanical properties of the individual microscopic phases (i.e., indentation depth ≪ characteristic size of the microscopic phases) [55]. Utilizing this criterion, the load function with a maximum load of 3000 μN was selected. The average indentation depth for this load function was around 200–400 nm for a 60 μm × 60 μm area containing all microscopic phases.

Nanoindentation tests were performed with a Hysitron Triboindenter UB1 system (Hysitron Inc. Minneapolis, MN) fitted with a Berkovich diamond indenter probe. The tip area function was calibrated by performing several indents with various contact depths on a standard fused quartz sample. Before starting the nanoindentation test, the sample

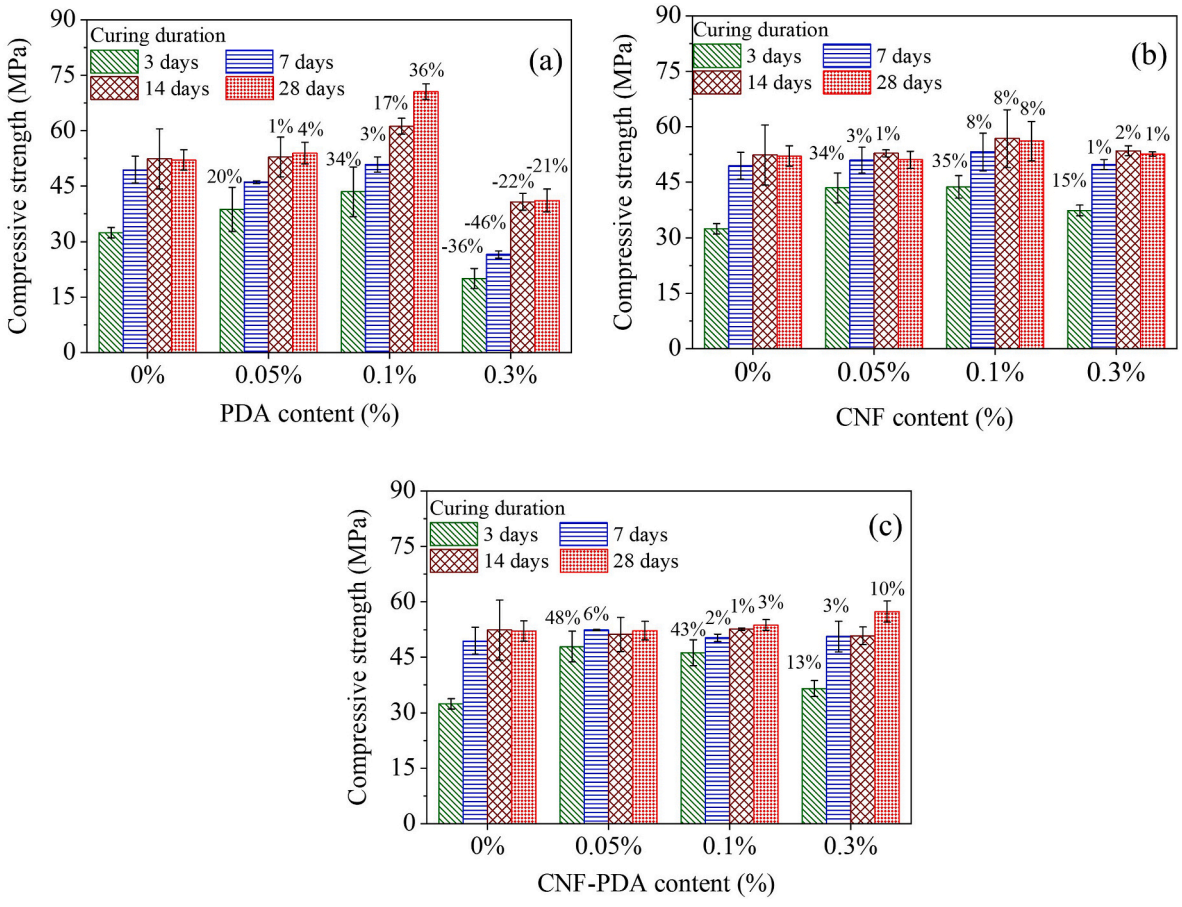

Fig. 2. Compressive strength of paste samples containing: (a) PDA, (b) CNF, and (c) CNF-PDA.

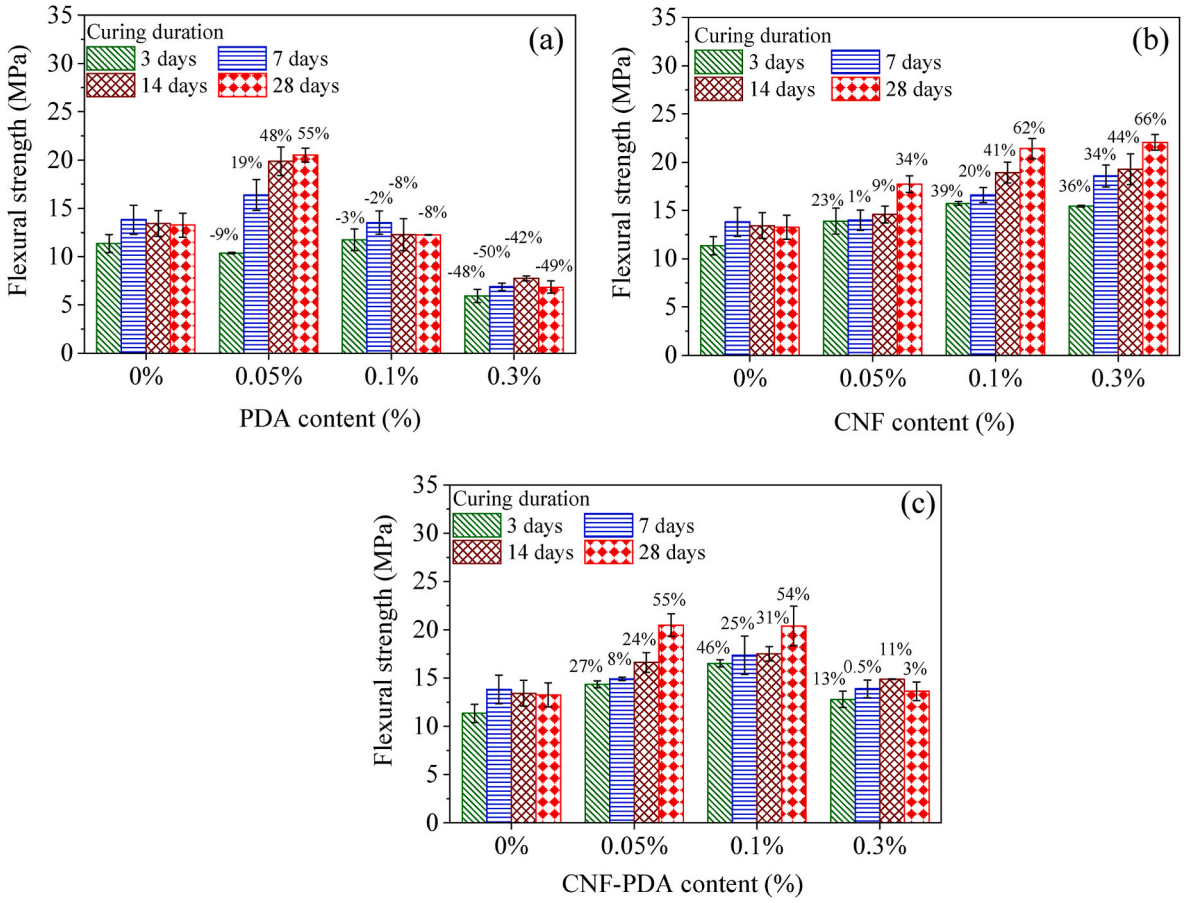

Fig. 3. Flexural strength of paste samples containing: (a) PDA, (b) CNF, and (c) CNF-PDA.

surfaces were scanned with the indenter tip to ensure adequacy of the test surface. In all cases, a surface RMS roughness lower than 80 nm (measured with the Berkovich tip) was detected over a 60 μm × 60 μm area. As such, the condition of the surface was considered adequate for performing the nanoindentation test.

Due to the heterogeneous nature of the microstructure containing multiple phases, a large number of indentations (around 220) needed to be performed on each specimen. To facilitate data interpretation, the experimental elastic modulus values were presented in the form of frequency distribution plots. These plots were, in turn, analyzed using the statistical deconvolution method [56,57] to estimate the intrinsic modulus of individual phases. These include the mean elastic modulus of each phase and their volume fractions, both of which were estimated based on the best fit of the experimental data with a limited number of Gaussian distribution function.

3. Results

3.1. Macro scale effects of biopolymers

3.1.1. Effects of biopolymers on the compressive and flexural strengths

The alkalinity of the OPC-slag system acts as an activator in the polymerization process of dopamine hydrochloride [33], as discussed in section 4. PDA formation is known to provide a dark grey appearance [18]. Cellulose-containing samples did not change color, whereas the PDA-containing samples changed to dark grey. Fig. 1 compares the effect of biopolymers on the physical appearance of the OPC-slag paste samples after demolding.

Fig. 2 (a) depicts the effects of PDA on compressive strength of the OPC-slag carbonated paste samples. After 3 and 28 d of carbonation-curing, the 0.05 wt% PDA samples show an increase in compressive strength of 20% and 4%, respectively, when compared to the control batch. After 3, 7, 14, and 28 d of carbonation-curing, 0.1 wt% PDA yields 34%, 3%, 17%, and 36% increase in compressive strength, respectively. It is to be noted that a higher concentration of PDA can bind more Ca^{2+} and impede the hydration and carbonation processes. As a result, less hydration and carbonation products were generated, resulting in lower compressive strength of the batches containing 0.3% PDA.

The effects of CNF on the carbonated OPC-slag binder composites are presented in Fig. 2 (b). The addition of 0.05 wt% and 0.1 wt% CNF boost early compressive strength (3 d of curing) by 34% and 35%, respectively. After 28 d of carbonation-curing, the addition of 0.1 wt% CNF enhance compressive strength by up to 8%. This enhancement is attributed to the channeling effect of CNF [58], which may have allowed faster diffusion of CO_2 in the matrix. CNF also provides nucleation sites for hydrated cementitious systems [45]. A similar mechanism can also accelerate carbonation reaction, and thus enhance the compressive strength of the composites.

The combined effects of CNF and PDA on compressive strength of an OPC-slag blended system are shown in Fig. 2 (c). It shows that 48% and 43% higher compressive strengths are achieved for 0.05 wt% and 0.1 wt % CNF-PDA after 3 d of carbonation-curing, respectively. After 28 d of curing, 0.3 wt% CNF-PDA shows a 10% increase in compressive strength.

Fig. 3 (a) represents the effects of PDA on flexural strength of the paste samples. The flexural strengths of the carbonated samples are increased by 18%, 48%, and 55% due to the addition of 0.05 wt% PDA after 7, 14, and 28 d of carbonation-curing, respectively. Previous research showed that PDA possesses higher tensile strength due to its polymer chain and side chains of polymerizable catechol monomers

Table 3
Statistical (*t*-test) analysis results (p-values) of compressive strength.

Biopolymers	Doses (%)	Curing durations			
		3 days	7 days	14 days	28 days
PDA	0.05%	0.0607	0.0834	0.3706	0.2062
	0.10%	0.0501	0.2734	0.0030	0.0009
	0.30%	0.0001	0.0003	0.0048	0.0275
CNF	0.05%	0.0054	0.2696	0.0685	0.3124
	0.10%	0.0014	0.1188	0.2026	0.1106
	0.30%	0.0047	0.4297	0.4140	0.3770
PDA-CNF	0.05%	0.0001	0.1026	0.1576	0.4796
	0.10%	0.0015	0.3414	0.0012	0.2120
	0.30%	0.0129	0.3538	0.0472	0.0205

*Note: p-values>0.05, no significant variation in strength compared to the control batch.

Table 4
Statistical (*t*-test) analysis results (p-values) of flexural strength.

Biopolymers	Doses (%)	Curing durations			
		3 days	7 days	14 days	28 days
PDA	0.05%	0.1059	0.0261	0.0017	0.0004
	0.10%	0.3067	0.2760	0.1428	0.0941
	0.30%	0.0009	0.0000	0.0012	0.0004
CNF	0.05%	0.0147	0.1546	0.1107	0.0012
	0.10%	0.0062	0.0050	0.0006	0.0003
	0.30%	0.0082	0.0008	0.0004	0.0017
PDA-CNF	0.05%	0.0119	0.0002	0.0080	0.0007
	0.10%	0.0036	0.0157	0.0023	0.0019
	0.30%	0.0496	0.0911	0.1368	0.3014

*Note: p-values>0.05, no significant variation in strength compared to the control batch.

[31], which is likely to contributed to the superior flexural strengths of the composites. A decrease in flexural strength is observed for higher PDA content, which could be due to the microcrack formation as observed later (section 3.2.4). Fig. 3 (b) shows flexural strength of the paste samples with the addition of CNF. Approximately, 23%, 39%, and 36% higher flexural strength is achieved on 3 d of carbonation-cured samples for 0.05, 0.1, and 0.3 wt% of CNF, respectively. For 28 d of curing, addition of 0.05, 0.1, and 0.3 wt% CNF show a flexural strength increase of 34%, 62%, and 66%, respectively. The increase in flexural strength is attributed to the crack-bridging ability of CNFs [43]. Fig. 3 (c) illustrates the combined effects of CNF and PDA on flexural strength. Around 55% higher flexural strength is achieved for 28 d of cured samples with 0.05 and 0.1 wt% CNF-PDA content. It is worth noting that combining CNF with PDA can enhance strength, even at higher doses (>0.05%) of PDA (Fig. 3 a and c).

3.1.1.1. Statistical (t-test) analysis of compressive and flexural strengths. The 'Two-sample *t*-test' statistical technique was used to evaluate the significant effect of biopolymers on compressive and flexural strength. The strength was compared with respect to the control batch (0% biopolymers). The test was conducted at a confidence level of 95%. Statistical p-values less than 0.05 implied a statistically significant difference between the two groups of samples and vice versa.

The '*t*-test' analysis results are provided in Table 3 for compressive strength. 0.1% PDA addition showed a statistically significant compressive strength increase in terms of p-values after 14 d and 28 d of curing. CNF and PDA-CNF addition significantly increase the early (3 d) compressive strength (p-values less than 0.05).

Table 4 shows the *t*-test results of flexural strength. 0.05% PDA addition showed significantly higher flexural strength at the later age of carbonation curing (14 d and 28 d), whereas CNF addition increased flexural strength from the early curing duration.

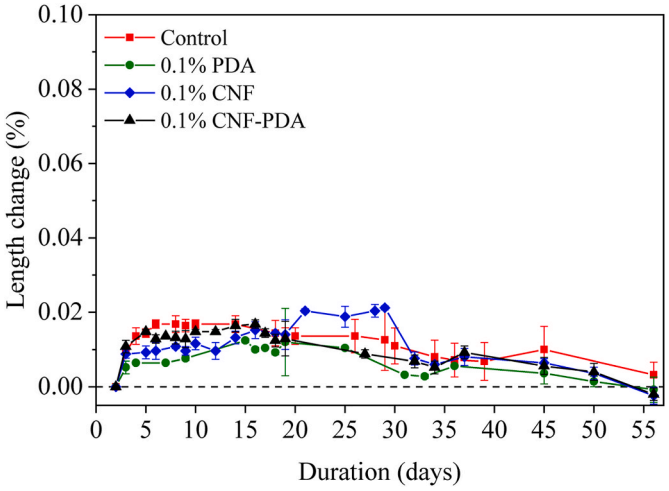

Fig. 4. Length change measurement of control, PDA, CNF, and CNF-PDA containing batches.

3.1.2. Effects of biopolymers on the dimensional stability of the carbonated composites

The length change of the carbonated composites, with and without biopolymers, is monitored for two primary reasons. First, CNF is well known for its role in reducing the shrinkage of hydrated cementitious composites [59]; and second, PDA has shown to induce cracks in the microstructure of the carbonated composites, which appeared to be due to shrinkage (details in section 3.2.4). Thus, it is deemed necessary to evaluate the roles of these biopolymers on the dimensional stability of the carbonated composites. The changes in the length of the slag-OPC mortars samples with and without the biopolymer addition are shown in Fig. 4. Carbonation of the OPC-slag blend appears to have increased the length by a maximum of 0.02%. During carbonation-curing, transformation of $Ca(OH)_2$ to $CaCO_3$ is known to yield 11.4% increase in solid volume [6], which is likely responsible for the observed length change. The addition of CNF and PDA reduces length change at the early age (before 10 d). However, the overall length change in these samples is also significantly less than those typically observed in OPC hydrated systems (around 0.08%) [60–62]. It can be concluded that the carbonation of the OPC-slag system, with or without biopolymers, doesn't significantly affect the dimensional stability of the mortar samples.

3.2. Microscale effects of biopolymers

3.2.1. Microstructural phase formations with and without biopolymers

The relative amounts of $Ca(OH)_2$ and chemically-bound water determined by the TGA are shown in Fig. 5 (a, b). $Ca(OH)_2$ decomposes between 400 and 500 °C, while chemically-bound water from calcium silicate hydrate (or Ca-modified silica gel) releases between 100° and 600 °C [7,63]. As illustrated in Fig. 5(a), the amounts of $Ca(OH)_2$ in the control batch decreases with carbonation duration, indicating that $Ca(OH)_2$ converts to $CaCO_3$. The batches containing PDA and CNF have higher proportions of $Ca(OH)_2$, indicating that these biopolymers either accelerated the hydration reaction and/or prevented the conversion of $Ca(OH)_2$ to $CaCO_3$. Chemically bound water content in all of the batches is nearly the same, except for that with 0.1 wt% PDA batch. This batch of samples had nearly a 30% higher chemically bound water content compared to the other batches, indicating a higher amount of gel formation in this batch.

The representative TGA plots in Fig. 6 (a) illustrate weight loss due to a gradual decrease in metastable $CaCO_3$ and the total $CaCO_3$. The amount of $CaCO_3$ and its relative metastable proportion are estimated from the TGA data [Fig. 6 (b, c)]. Several prior research have discovered that $CaCO_3$ decomposes between 200 and 750 °C [64–66]. The gradual

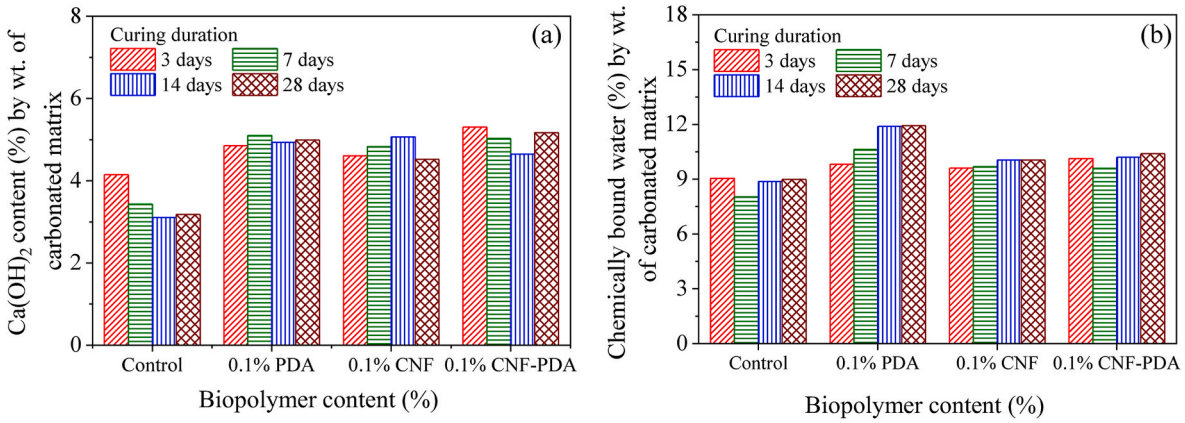

Fig. 5. (a) $Ca(OH)_2$ content (%) and (b) chemically bound water (%) content as a function of biopolymer addition.

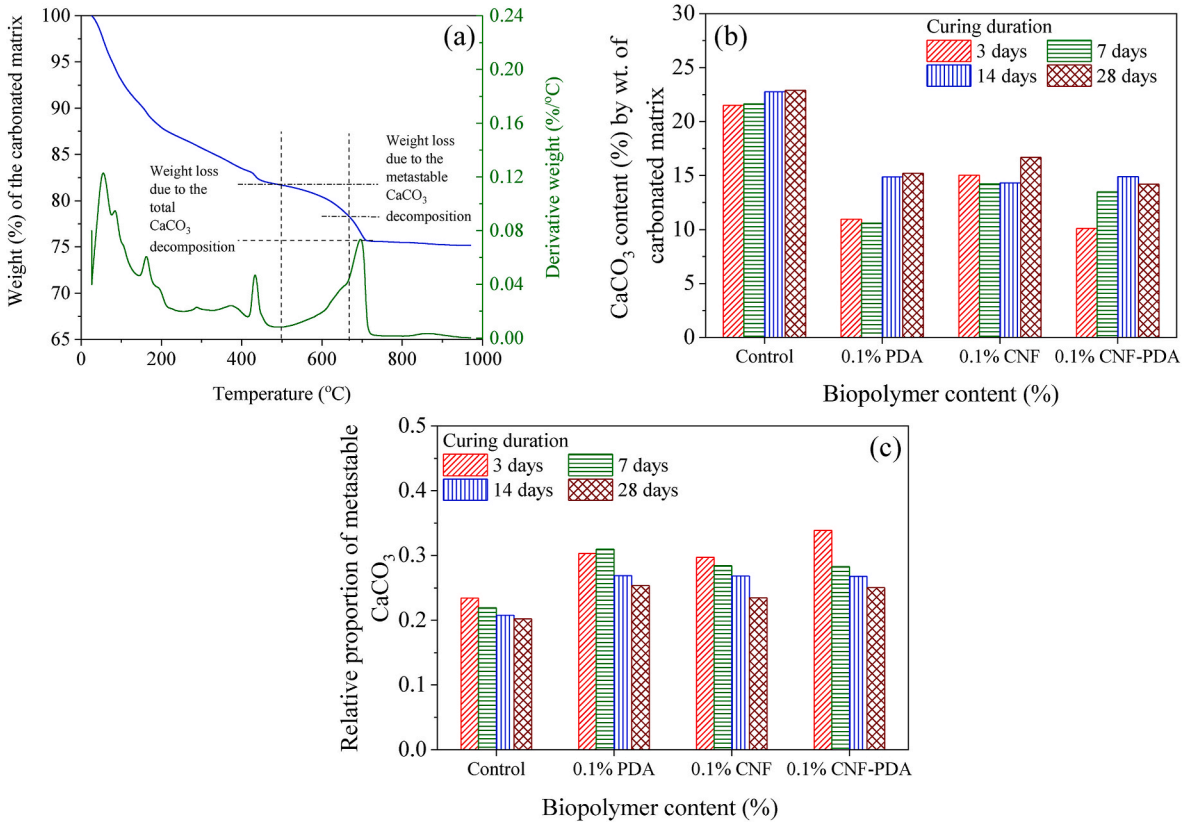

Fig. 6. (a) Representative TGA weight loss profile illustrating the relative loss of mass due to the decomposition of metastable and total $CaCO_3$, (b) $CaCO_3$ yield (%) as a function of biopolymer amounts, and (c) Relative yield of metastable $CaCO_3$ as a function of biopolymer amounts.

weight loss in this range is due to the decomposition of amorphous $CaCO_3$ (ACC), aragonite, and vaterite [11]. These crystalline forms are commonly known as 'metastable $CaCO_3$' and will be addressed as '$mCaCO_3$' for the remainder of this article. The sharp weight loss from 650 to 750 °C is due to the decomposition of calcite [66]. For the determination of the $CaCO_3$ amount, weight loss from 500 to 750 °C has been considered in this study. To avoid the influence of calcium silicate hydrate (or Ca-modified silica gel) and $Ca(OH)_2$, weight loss between 200 and 450 °C has not been taken into account, when estimating $CaCO_3$ amount. It is worth noting that PDA decomposes between 620 and 700 °C [17]. However, because the concentration of PDA was insignificant, weight loss due to PDA can be considered negligible in comparison to the $CaCO_3$ weight loss hence had been disregarded.

Fig. 6 (b) shows the amounts of total $CaCO_3$ (%) per weight of the carbonated composites for different dosages of biopolymers. The addition of either PDA or CNF reduces the amounts of $CaCO_3$ formation in the matrix. Specifically, the 0.1 wt% PDA-containing batch has 50%, 51%, 35%, and 33% lower $CaCO_3$ amounts after 3, 7, 14, and 28 d of curing, respectively (compared to the control batch). Such reduction can be attributed to its affinity for Ca^{2+} ions. Previous studies have shown that PDA stabilizes the $mCaCO_3$ and blocks transition to the calcite phase [17]. That study also suggested that due to the presence of catechol groups in PDA keeps the $mCaCO_3$ together, and the affinitive interaction between the Ca^{2+} and the catechol prevents dissolution of $mCaCO_3$ and the subsequent recrystallization of calcite. This Ca^{2+} ion affinity also hinders formation of $CaCO_3$ during the carbonation process. Additionally, formation of $mCaCO_3$ reduces the extent of carbonation as explained in an earlier study [11].

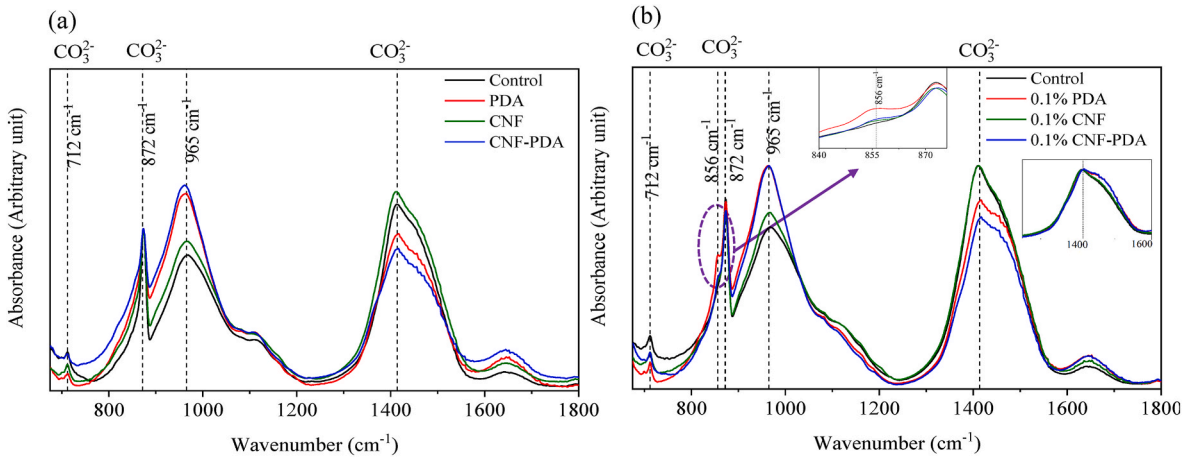

Fig. 7. FTIR spectra after curing duration of (a) 3 days, and (b) 28 days.

CNF possesses hydroxyl (OH^-) and carboxyl ($COOH^-$) moieties having oxygen atoms with unpaired electrons [67]. These unpaired electrons can bind positively charged Ca^{2+} ion and therefore, reduce the free Ca^{2+} availability resulting in a decrease in $CaCO_3$ formation. Thus, the paste samples containing 0.1 wt% CNF show 30%, 34%, 37%, and 17% lower $CaCO_3$ formation after 3, 7, 14, and 28 d of curing, respectively (compared to the control batch) [Fig. 6 b]. However, the CNF containing batches contain higher amounts of $CaCO_3$ compared to the PDA containing ones. Fig. 6 (c) shows $CaCO_3$ formation in OPC-slag samples with 0.1 wt% CNF-PDA. The combination of both CNF-PDA reduced $CaCO_3$ formation by 53%, 38%, 35%, and 38% after 3, 7, 14, and 28 d of curing, respectively.

The relative proportions of $mCaCO_3$ is estimated from the ratio of the weight loss from decomposing $mCaCO_3$ (500–650 °C) and calcite (650–750 °C) [11]. Fig. 6 (c) shows relative proportion of $mCaCO_3$. After 3 d of curing, the batch containing 0.1 wt% CNF-PDA shows a 45% increase in $mCaCO_3$, while the batch with 0.1 wt% PDA yields a 26% increase in $mCaCO_3$ after 28 d of curing. Thus, PDA is more effective in producing $mCaCO_3$ even after prolonged carbonation, whereas CNF-PDA is more effective at producing $mCaCO_3$ during short carbonation durations. Previous research has shown that the formation of a higher amount of $mCaCO_3$ offers superior mechanical performance of the carbonated composites [11]. The formation of relatively higher amounts of $mCaCO_3$ due to the addition of biopolymers can be considered as one of the underlying causes for achieving superior flexural strength (up to 0.05 wt% dosage) (Fig. 3).

3.2.2. *Identifying different polymorphs of $CaCO_3$ formed during carbonation reaction*

The formation of carbonate polymorphs in OPC-slag binders with and without biopolymers was investigated with FTIR and XRD. The peaks in the 800 cm^{-1} to 1200 cm^{-1} range are prominent, which likely are present due to the asymmetric and stretching vibration (ν_3) of the Si–O bond [68,69]. The exact location of these peaks depends on the Ca/Si ratio [68]. The band of calcium silicate hydrate (C–S–H) gel can be observed at around 950 cm^{-1} and this is due to the Si–O stretching vibration (ν_3) of the Q^2 tetrahedron [68,70–72]. The response between 1400 cm^{-1} to 1500 cm^{-1} is due to asymmetric stretching (ν_3) of CO_3^{2-} and between 872 cm^{-1} and 856 cm^{-1} is due to out-of-plane and in-plane bending vibration (ν_2) of CO_3^{2-} [66,69]. The bending peak vibration around 1639 cm^{-1} is likely because of the presence of $Ca(OH)_2$ and chemically-bound water [69,73]. The C═C resonance vibration of the aromatic ring and the N–H bending vibrations of the amide groups in PDA occur at 1600 cm^{-1} [19]. This PDA peak mostly overlaps with the OH^- peak, and thus is challenging to uniquely distinguish with FTIR analysis.

Fig. 7 shows the FTIR spectra of the 3 and 28 d carbonation-cured samples. All the samples after 3-d of carbonation curing show likely

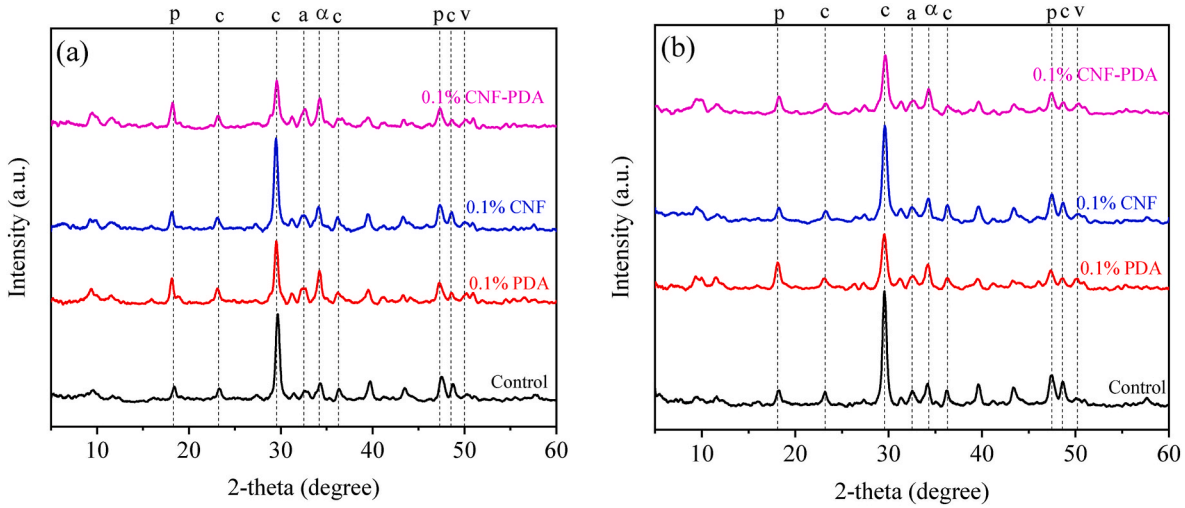

Fig. 8. XRD patterns after curing duration of (a) 3 days and (b) 28 days. Following descriptors are used to identify resonance for typical crystalline phases; p: portlandite, a: aragonite, c: calcite, α: unreacted alite, v: vaterite.

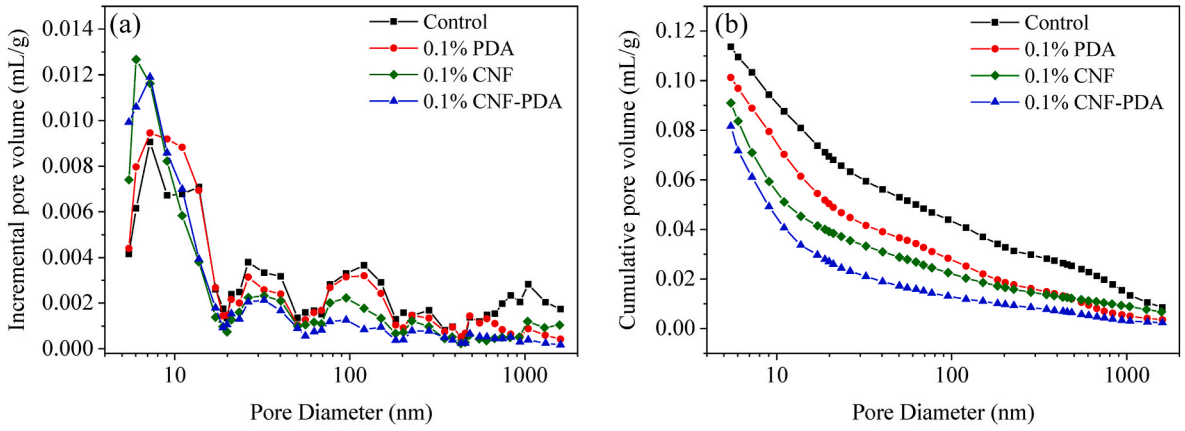

Fig. 9. Effects of CNF and PDA on pore size distribution of OPC-slag blended of 28 days carbonated composites.

Table 5
Effects of biopolymers on the pore structure of 28-day carbonated samples as obtained by the MIP.

Sample Name	Porosity (%)	Total Pore area (m^2/g)	Med. Pore Dia (nm)	Avg. Pore Dia (4V/A) (nm)
Control	20.45	21.97	38.18	20.70
0.1% PDA	17.93	24.51	19.74	16.52
0.1% CNF	16.47	27.16	13.57	13.41
0.1% CNF-PDA	14.74	28.16	10.99	11.59

formation of calcite, as elicited by the presence of 712 and 872 cm^{-1} absorbance peaks [Fig. 7 (a)]. For 28 d curing, the 0.1 wt% PDA-containing samples show a peak at 856 cm^{-1}, which is a characteristic peak for aragonite. Batches containing CNF and CNF-PDA indicate a low level of aragonite content. However, the sharp resonance at 1414 cm^{-1} is likely due to the presence of calcite, and the peak broadening is due to the metastable $CaCO_3$ (i.e., vaterite, ACC) presence [74,75]. The control and CNF-containing batches show a sharp peak at around 1414 cm^{-1}. On the other hand, both PDA-containing batches show peak broadening (as shown in inset image in Fig. 7(b)). This indicates that addition of PDA formed metastable $CaCO_3$ (peak broadening). Previous studies have reported formation of vaterite in PDA-containing batches [19,20,76]. In the FTIR analysis, in-plane bending and stretching vibrations for

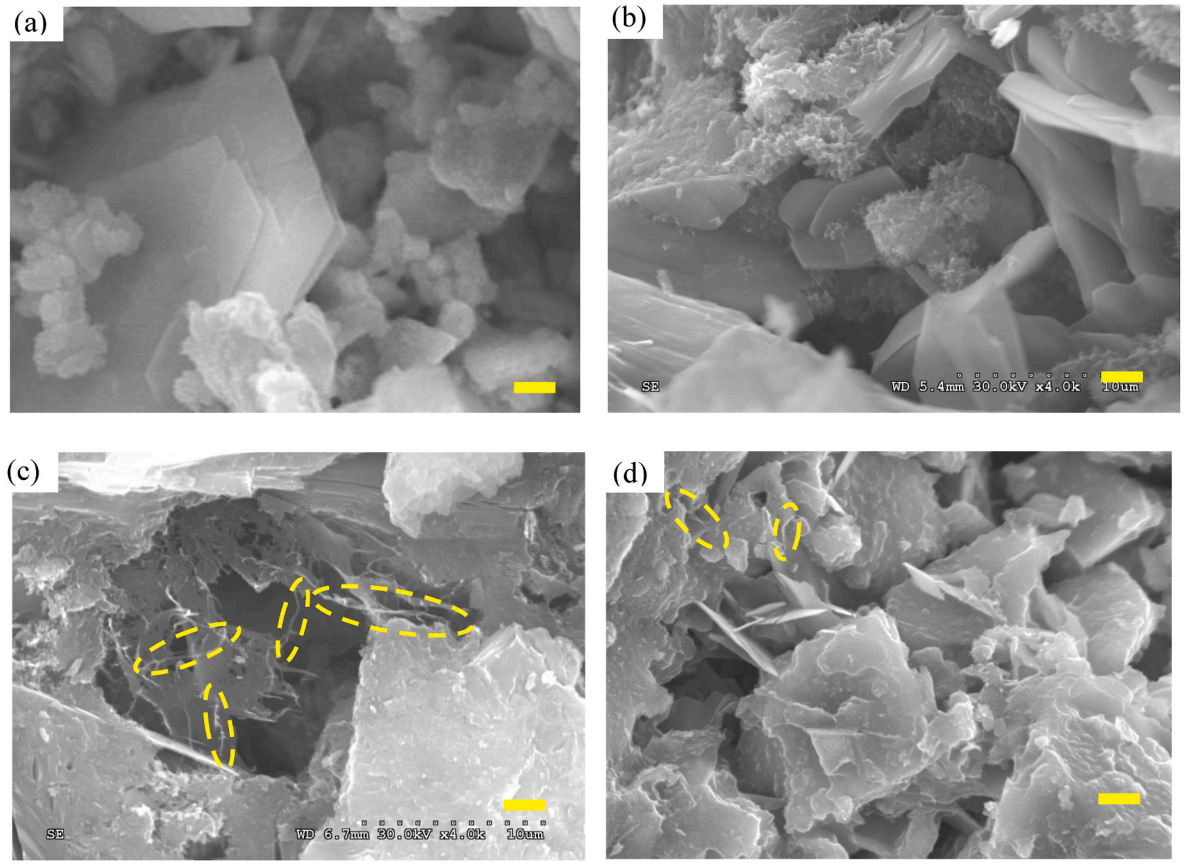

Fig. 10. SEM/SE images of carbonated paste samples containing (a) 0% biopolymer (control), (b) 0.1 wt% PDA, (c) 0.1 wt% CNF, and (d) 0.1 wt% CNF-PDA. The yellow scale bar represents 2 μm. (For interpretation of the references to color in this figure legend, the reader is referred to the Web version of this article.)

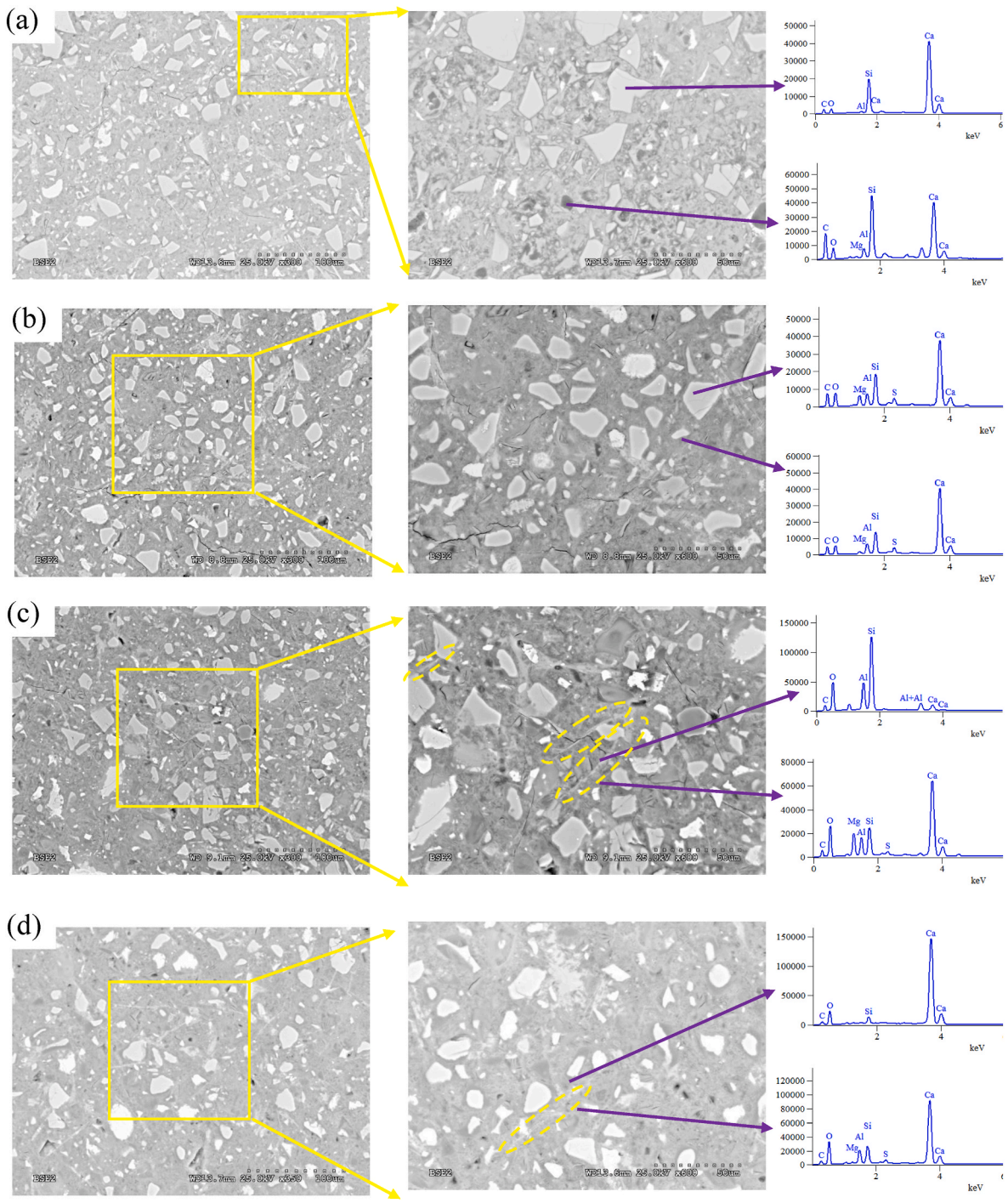

Fig. 11. Back scattered images of (a) control, (b) 0.1 wt% PDA, (c) 0.1 wt% CNF, and (d) 0.1 wt% CNF-PDA after 28 days of carbonation-curing.

vaterite often overlap with aragonite and amorphous $CaCO_3$—thus the exact polymorph of the metastable $CaCO_3$ cannot be concluded from the observation.

Fig. 8 shows the XRD patterns of the 3 and 28 d samples with and without biopolymers. Portlandite, calcite, and aragonite are the major crystalline phases in these carbonated systems. The intensity of portlandite was higher for the batches containing PDA, showing that incorporation of PDA reduces the rate of carbonation and preserves the hydration reaction products. The TGA investigations also confirms this observation. Furthermore, the intensity of calcite is reduced with biopolymer addition. This postulates that biopolymers reduce the formation of calcite and increase the same of $mCaCO_3$. The calcite intensity increases with carbonation duration (from 3 to 28 d of carbonation-curing) for the control batch. The calcite intensity does not increase in the PDA-containing samples, indicating that PDA has a carbonation retarding influence, similar to that of amino acids [21–23].

3.2.3. *Effects of biopolymers on microscale pore size distribution*

Pore structures of 28 d cured cement paste samples obtained by MIP are presented in Fig. 9 and in Table 5. The addition of biopolymers has significantly reduced the total porosity and average pore diameter compared to the control batch. Table 5 shows that the total porosity of the paste samples is reduced by 13%, 20%, and 28% due to the addition of 0.1 wt% PDA, CNF, and CNF-PDA, respectively. The addition of

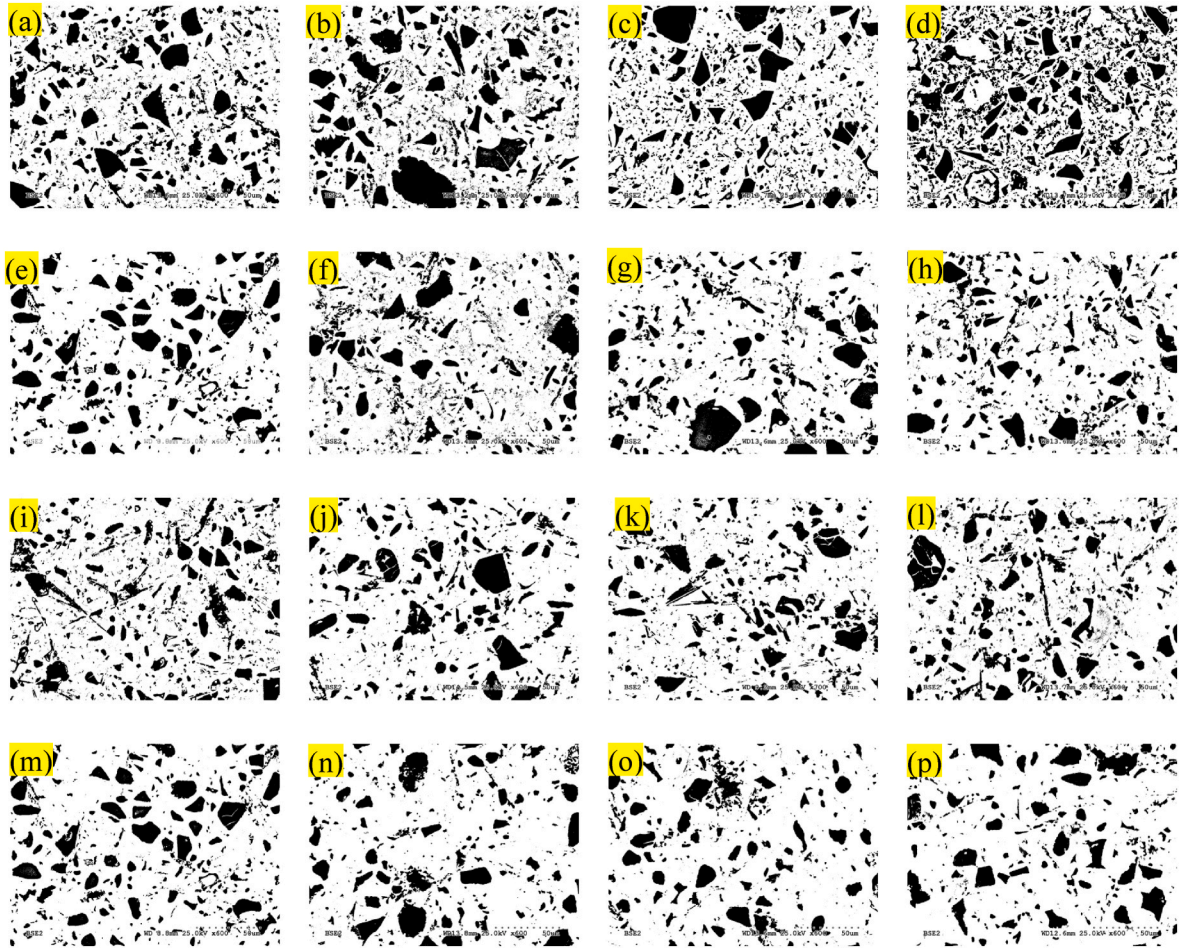

Fig. 12. Examples of the BSE images of 28 days cured samples after processing through ImageJ. (a–d) control, (e–h) 0.1 wt% PDA, (i–l) 0.1 wt% CNF, and (m–p) 0.1 wt% CNF-PDA.

biopolymers increases the formation of $mCaCO_3$, as observed from the FTIR and TGA experimental data. This $mCaCO_3$ has a lower density than calcite, resulting in less porosity and denser microstructure [52,77]. Such a reduction in porosity can contribute to higher mechanical performances as observed in section 3.1. Apart from porosity, the average pore diameter also moved toward a lower diameter, indicating pore size refinement. The combination batch of CNF-PDA yields less porosity and lower pore diameter compared to the batches containing only PDA or CNF.

3.2.4. SEM observations

Fig. 10 shows the microstructure of carbonated OPC-slag, with and without the addition of biopolymers after 28 d of curing. Fig. 10 (a) depicts the formation of $Ca(OH)_2$ in the control batch. In the 0.1% PDA-containing batch, vaterite plate and CSH gel or Ca-modified silica gel are visible, as illustrated in Fig. 10 (b) and in Fig. S1(b). The CNF fibers emerging from cement paste are shown in Fig. 10 (c) and Fig. S1(c). CNF fibers are covered with a silica gel as shown in Fig. 10 (d).

Backscattered scanning electron (BSE) microscopy images of 28-d-cured polished samples are shown in Fig. 11. The unreacted OPC and slag particles as well as the uniformly distributed pores are visible in Fig. 11 (a). Fig. 11 (b) shows that OPC-slag with 0.1 wt% PDA incorporation has lower porosity and fewer unreacted OPC-slag particles. However, several microcracks are observed across these PDA-containing samples. These microcracks could form during the *in-situ* polymerization of dopamine to PDA in these samples. These microcracks may have worked as flaws in the system resulting in reduced flexural strength as observed in Fig. 3 (a). Thus, the addition of PDA has increased the formation of reaction products but also resulted in microcracks throughout the matrix. Fig. 11 (c) shows a significantly dense microstructure caused by the 0.1 wt% CNF addition when compared to the control batch. The CNF can be easily visible throughout the microstructure. Additionally, EDS illustrates the deposition of a layer of $CaCO_3$ on CNF. Fig. 11 (d) shows a dense microstructure of the batch containing 0.1 wt% CNF-PDA. Only PDA-containing samples exhibit microcracks, whereas CNF-PDA containing samples have cracks that have been bridged by CNF also reported in several past articles [10–12].

Table 6
BSE image analysis results of 28 days cured samples.

Sample Name	Average unreacted cement (%)	Standard Deviation (±)
Control	29.083	2.238
0.1% PDA	21.470	0.944
0.1% CNF	21.295	0.969
0.1% CNF-PDA	18.818	2.085

Additionally, BSE images are evaluated with an image analysis software (ImageJ) [78] and these images are translated into a binary system with identification of unreacted binders and reaction products. The relative amounts of unreacted particles are then estimated. Fig. 12 shows dark contrast areas denoting unreacted sites and lighter contrast areas signifying reacted areas. Based on the analysis, control, 0.1 wt% PDA, CNF, and CNF-PDA yielding 29.08%, 21.47%, 21.3%, and 18.82% unreacted products, respectively as shown in Table 6. This implies that the addition of biopolymers has increased the degree of reaction of the binder compared to that of the control batches. This finding confirms the

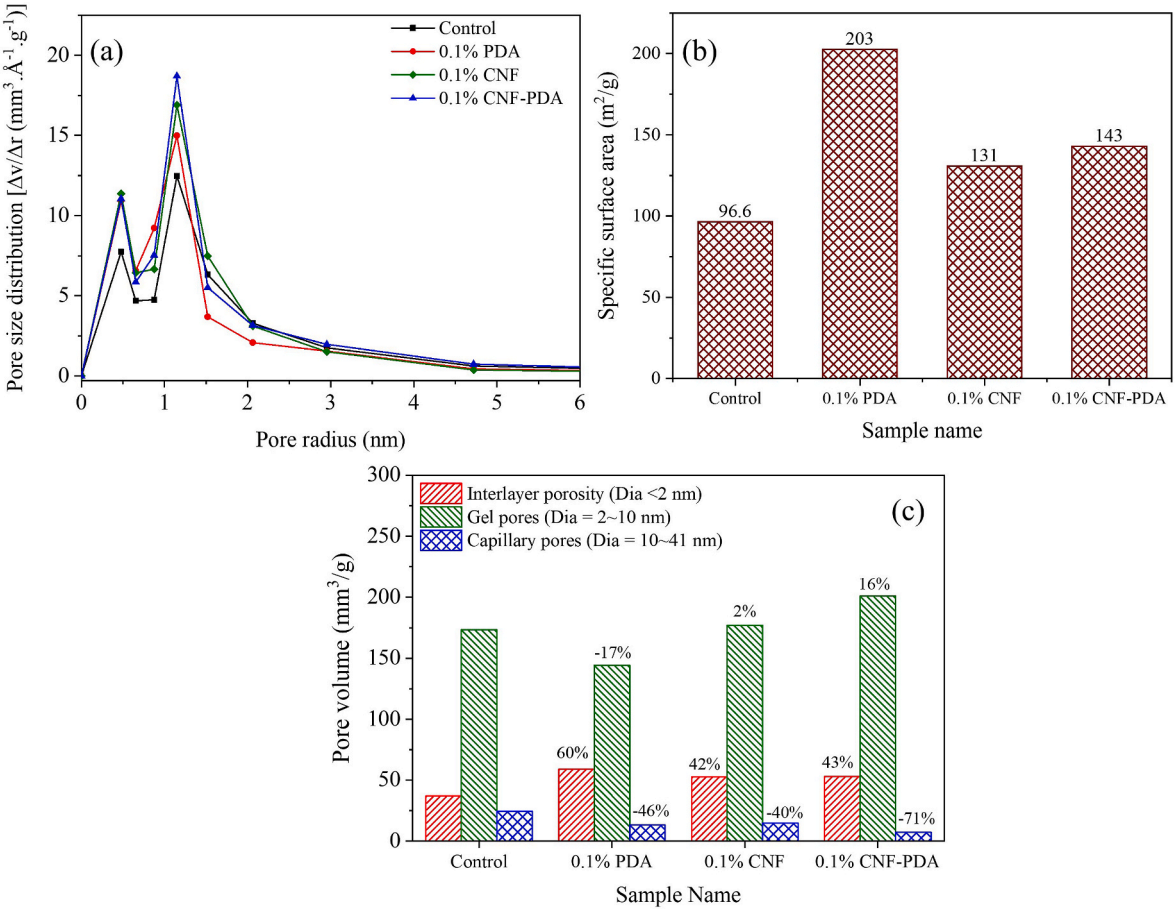

Fig. 13. (a) Pore size distribution, (b) specific surface area, and (c) volume of different pore categories of OPC-slag binder, with and without biopolymer additives.

pore size analysis obtained from MIP (Fig. 9) and DVS (Fig. 13), which shows densification of the microstructure due to the addition of biopolymers; a likely result of reaction product generation.

3.3. Nano scale effects of biopolymers

3.3.1. Nano-porosity measurements using DVS

Compared to MIP or nitrogen sorption techniques, DVS is generally considered to be more preferred for characterizing and investigating meso-scale and gel pore structures in cementitious materials, especially those containing CSH or Ca-modified silica gels [52]. In this study, the specific surface area (S_{BET}) of carbonated composites was determined by the BET method [50], and pore size distribution was determined using the BJH model [51]. The calculation of the BET and BJH methods was based on previous studies [52,53].

The pore size distributions of 28 days carbonated OPC-slag binder with and without biopolymers are shown in Fig. 13. This graph reveals two significant peaks in the pore size distribution of a carbonated system, at around 11.4 Å and 5 Å radius. The peaks at 11.4 Å correspond to the porosity of the interlayers in CSH/Ca-modified silica gel structures. No peak shift is found because of the biopolymer addition, indicating that CNF and PDA does not affect the silicate structure. However, the inclusion of biopolymers results in an increase in interlayer porosity, indicating higher amounts of CSH/Ca-modified silica gel formation. The specific surface areas of carbonated slag-OPC composites, with and without biopolymers, are shown in Fig. 13 (b). The specific surface area corresponds to the number of fine pores accessible to water [53]. The specific surface area (S_{BET}) of fully hydrated cement paste is approximately 100–200 m^2/g [79]. The addition of PDA, CNF, and CNF-PDA increases specific surface area of the carbonated composites by 110%, 36%, and 48%, respectively. PDA suppresses the agglomeration of $CaCO_3$, resulting in a greater amount of $mCaCO_3$ than calcite. The $mCaCO_3$ phases, specifically vaterite and ACC, have larger surface area than the calcite phase, because of their lower density [11,52,80]. Additionally, as observed from the image analysis (section 3.2.4), PDA increases the degree of reaction. Both aforementioned factors contribute to the higher specific surface area (S_{BET}) yield for the PDA-containing sample (compared to other batches). The pore volume distribution of the carbonated samples is presented in Fig. 13 (c). The addition of PDA results in a 60% increase in interlayer porosity and a 16% increase in gel porosity in the OPC-slag carbonated composites (compared to the control batch). Furthermore, it reduces capillary porosity by 71%. Thus, the combination of PDA and CNF results in densification of the microstructure.

3.3.2. Nano-mechanical properties

Grid indentation is applied to each sample over two 60 μm × 60 μm sections, resulting in a total of 220 indentations. Fig. 14 shows the elastic modulus frequency distribution for the control, 0.1 wt% CNF, PDA, and CNF–PDA batches. The cumulative frequency distribution functions (CDF) of the elastic modulus (E) are then statistically deconvoluted, assuming a normal frequency distribution function of elastic moduli for all the individual microscopic phases, to obtain quantitative comparability [56,57]. For all the microstructural phases, this deconvolution method generates a probability distribution function (PDF) of the elastic modulus (i.e., the mean and corresponding standard deviation). However, the deconvolution procedure is chosen in this study for the elastic modulus range of 0–100 GPa, to primarily focus on the reaction products.

According to previous reports, the elastic moduli of Ca-modified

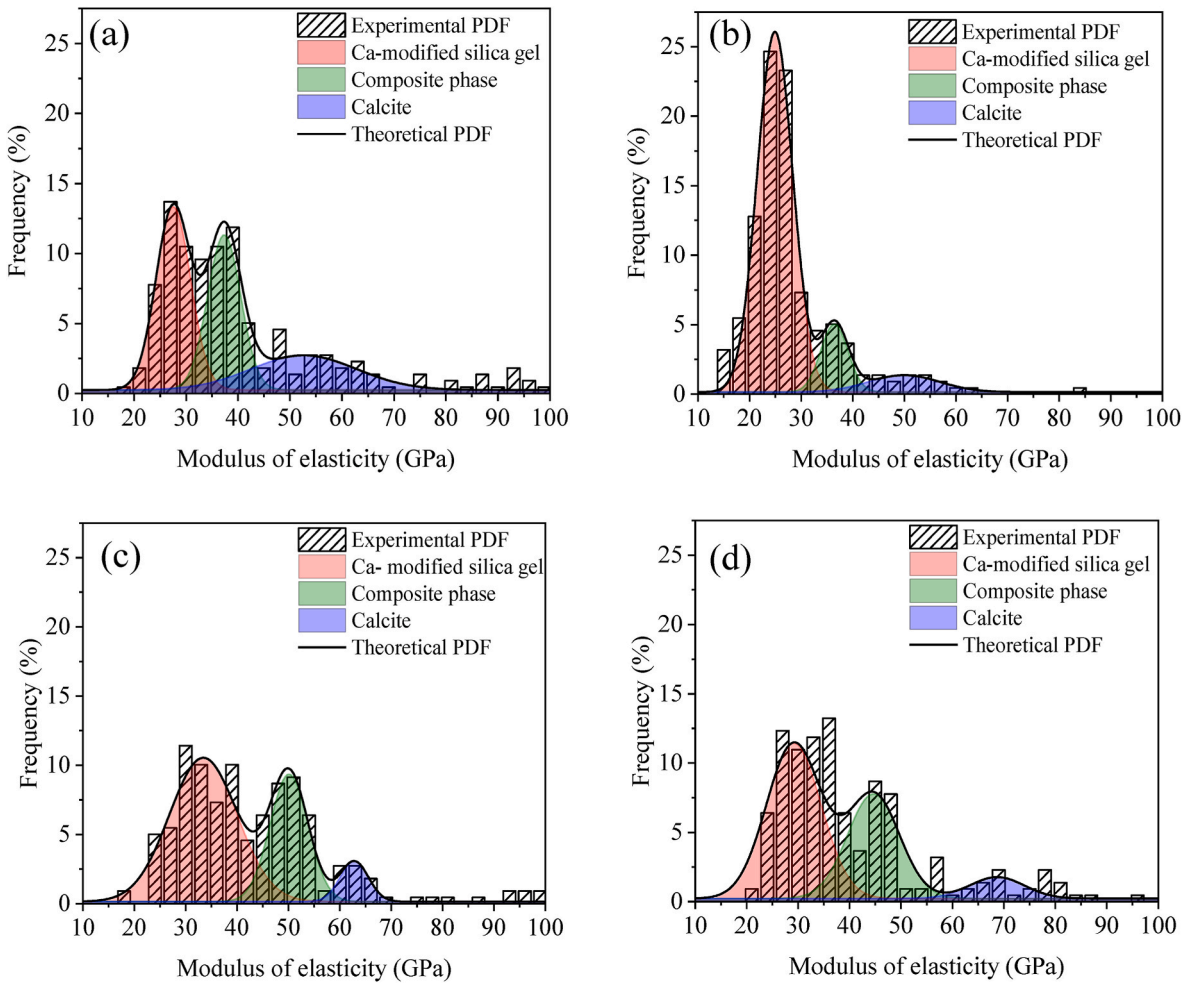

Fig. 14. Percent frequency versus elastic modulus of (a) control, (b) 0.1% PDA, (c) 0.1% CNF, and (d) 0.1% CNF and PDA after 28 days of carbonation-curing.

silica gel and $CaCO_3$ present in CO_2-cured cementitious composites are around 32–42 GPa and 54–79 GPa, respectively [52,57,81–83]. Additionally, carbonated calcium silicates form a composite phase by the mixture of $CaCO_3$ and Ca-modified silica gel, which has a mean elastic modulus of around 40 GPa [81]. $Ca(OH)_2$ also has an average elastic modulus of around 40 GPa [84]. Interestingly, $CaCO_3$ can exhibit a wide range of elastic moduli due to the formation of different polymorphs. The elastic moduli of aragonite, vaterite, and calcite have been determined to be 39, 67, and 72 GPa, respectively [85]. The elastic modulus of ACC remains unknown. Considering that vaterite and the composite phase have similar elastic moduli, it is not possible to separate these phases by statistical deconvolution. The frequency distribution of the control batch is shown in Fig. 14 (a), and it contains 42% Ca-modified silica gel, 34% $mCaCO_3$ with the composite phase, and 24% calcite. As illustrated in Fig. 14 (b), the 0.1% PDA addition sample contains 80% Ca-modified silica gel/CSH, 12% $mCaCO_3$ with composite phase, and 8% calcite. The 0.1% CNF samples include 62% Ca-modified silica gel/CSH, 31% $mCaCO_3$ with composite phase, and 7% calcite, respectively (Fig. 14 (c)). In the case of the CNF-PDA batch, it contains 56%, 36%, and 8% Ca-modified silica gel/CSH, $mCaCO_3$ with composite phase, and calcite, respectively as shown in Fig. 14 (d). The addition of PDA significantly increases the amount of Ca-modified silica gel/CSH in this carbonated binder matrix and decreases the formation of calcite. The decreased formation of calcite due to the addition of PDA confirms the observations from FTIR and TGA. Addition of CNF-PDA also enhanced the production of silica gel and $mCaCO_3$.

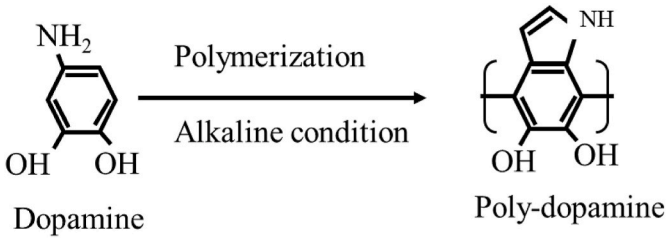

Fig. 15. Dopamine polymerization in alkaline conditions; adopted from Ref. [18].

3.4. Discussion

The addition of PDA is found to have improved flexural strength and early-age compressive strength of the carbonation-cured Ca-based cementitious composites. The improvement in mechanical performance due to the addition of PDA can be attributed to the following factors:

(i) *In-situ polymerization of PDA:* The biopolymer develops a network within the binder matrix due to self-polymerization and propagates through the solid phases in alkaline conditions (Fig. 15). This alkaline state allows for deprotonation of phenolic groups found in dopamine hydrochloride molecules, resulting in negatively charged sites along the polymer's backbone. We hypothesize that during the polymerization process (Fig. 15), negatively charged sites preferentially electrokinetically interact with positively charged sites within the binder structure, such as Ca^{2+} and Al^{3+} sites, forming an interconnected network of

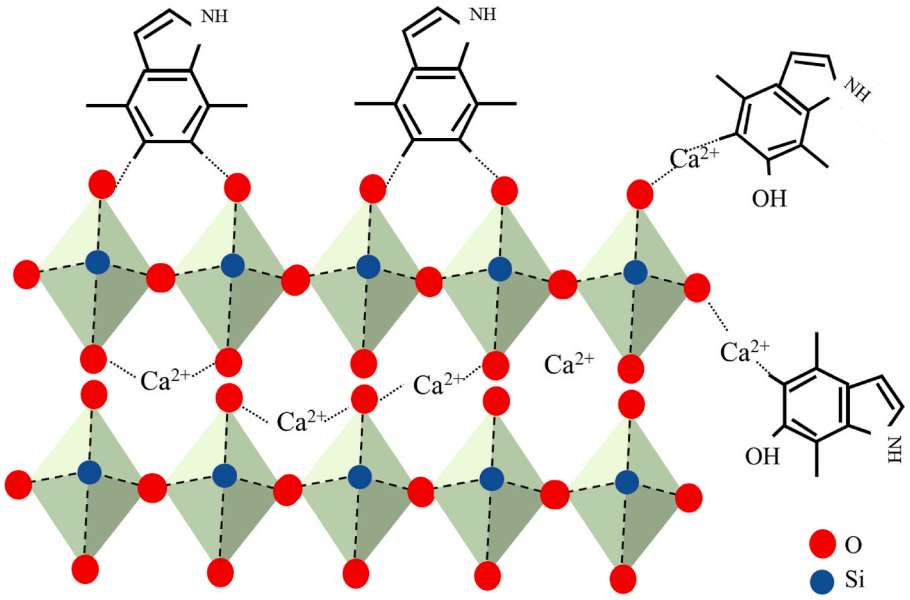

Fig. 16. Schematic representing hypothetical interaction of PDA moieties with the silicate chain of C–S–H and Ca-modified silica gel.

polymer-binder composites. This integrated network contributes to a denser microstructure and higher mechanical performance. The improved mechanical performance could be attributed to the strong chemical interaction between the polymer backbone and the binder matrix, as well as the intrinsic higher strength of the PDA fibers.

(ii) *Bonding among PDA and binding phases:* Carbonation-cured OPC-slag binder produce $Ca(OH)_2$, $CaCO_3$, CSH gel, and Ca-modified silica gel. CSH gel has a porous, non-stoichiometric, tobermorite-like structural silicate chain layer with a silanol (Si–OH) group [86]. A previous study has shown that the OH^- group in PDA could result in a bidentate hydrogen bonding interaction with the silicate chains [86,87]. Some partially charged OH^- group in PDA can also result in possible surface adsorption of Ca^{2+}. PDA and CSH, as well as Ca-modified silica gel, form a strong bond as a result of these interactions. Such high interactions increase the mechanical performance of the PDA-containing batches. This mechanism is illustrated in Fig. 16.

(iii) *Increased degree of reaction:* The addition of PDA also results in a higher degree of reaction and a denser microstructure formation of the carbonation matrix, as confirmed by the SEM/BSE image, MIP, and DVS pore size analyses. However, the amounts of $CaCO_3$ formation are reduced due to the binding of Ca^{2+} by the PDA.

In the case of CNF addition, the flexural strength of the carbonated composites are improved because of two likely reasons: (a) CNF bridged micro- and macro-cracks, and thus enhanced the flexural strength of the matrixes [45]; and (b) the inclusion of CNF is also observed to produce a denser matrix due to a higher degree of reaction as observed from the pore size and BSE image analyses. The negatively charged $COOH^-$ surface sites of CNF can also electrokinetically interact with Ca^{2+}, which can reduce formation of $CaCO_3$ in presence of CNF.

However, the effects of those biopolymers in carbonated binders are more pronounced in early curing days. As those biopolymers increase the reactions, we hypothesize that most of the reactions happened in the early curing days. Thus, the effects of those biopolymers are stronger on early curing days. Besides, PDA and CNF increased the nano porosity (pore size lesser than 10 nm) and decreased the microporosity (pore size higher than 10 nm), as shown in Figs. 9 and 13.

A comparison with a previous study on the application of amino acids as additives for carbonated composites [11] reveals that the addition of amino acids was more effective in increasing flexural strength (106%) and compressive strength (48%) compared to the biopolymers studied here. However, this earlier study was performed using wollastonite, which is generally considered as a non-hydraulic calcium silicate. On the other hand, OPC with a slag binder can be considered as a hydraulic calcium silicate binder. Thus, the effectiveness of biopolymer addition during the carbonation of these materials can be different, and therefore require additional investigation for obtaining a direct comparison.

4. Conclusions

This study provides a detailed investigation of the effects of PDA and CNF on Ca-based carbonated cementitious composite properties. This study yields the following conclusions.

(i) PDA increases the formation of metastable $CaCO_3$ in CO_2-cured composites by 26% and reduces total carbonate formation by 50%. The addition of CNF also reduces the mass of carbonates formed in the matrix compared to those in the control batch by 37%.

(ii) The carbonated composites containing biopolymers have higher amounts of nano-porosity compared to the control batch, indicating a denser microstructure formation in these composites. Both BSE/SEM images and pore-size distribution analysis indicate that the addition of biopolymers increases the degree of reaction in the binders.

(iii) All the dosage and combinations of biopolymers enhance compressive strength by nearly 35% after the early-stage carbonation curing (i.e., of 3 days). However, effects of these biopolymers on compressive strength after 28 days curing is minimal.

(iv) The significance of combining PDA with CNF is that CNF can potentially arrest micro-cracks caused by PDA addition.

(v) Overall, the optimum dosage for PDA addition is 0.05 wt%, as it improves flexural strength by 55% after 28 days of curing. The addition of CNF up to 0.3 wt% improves flexural strength by 66% after 28 days of curing. The benefit of combining CNF and PDA are three folds: (a) it improves early-age (i.e., 3 days curing) compressive strength by nearly 48%, (b) it offers the densest microstructure among all the batches, which can be advantageous for improving durability performance, and (c) it offers the highest degree of reaction.

In summary, this study finds that the application of either PDA or CNF biopolymer in carbonated composites can be beneficial in three aspects, i.e., (a) improvement in early-age (i.e., 3 days) compressive and flexural strength, (b) flexural strength enhancement of the composites, and (c) a decrease in total porosity and reduction in critical pore size.

Declaration of competing interest

The authors declare that they have no known competing financial interests or personal relationships that could have appeared to influence the work reported in this paper.

Data availability

Data will be made available on request.

Acknowledgement

This work was conducted with partial funding support from the US National Science Foundation (NSF # ECI - 2028462), Defense Advanced Research Projects Agency (DARPA)- Young Faculty Award (#W911NF2010308) for Dr. Warda Ashraf. All opinions, findings, and conclusions or recommendations expressed in this material are those of the authors and do not necessarily reflect the views of the funding agencies. The authors gratefully acknowledge the assistance of graduate student Adhora Tahsin and undergraduate student Sushmita Shrestha in some experiments.

Appendix A. Supplementary data

Supplementary data to this article can be found online at https://doi.org/10.1016/j.cemconcomp.2022.104766.

References

[1] U.S. energy-related carbon dioxide emissions fell in 2019, mainly in electric generation - today in Energy - U.S. Energy Information Administration, (EIA) (2021). https://www.eia.gov/todayinenergy/detail.php?id=45836. n.d.
[2] E. Assessment, TRENDS IN GLOBAL CO 2 and TOTAL GREENHOUSE GAS 2020 Report, 2020.
[3] M. Mahoutian, Z. Ghouleh, Y. Shao, Carbon dioxide activated ladle slag binder, Construct. Build. Mater. 66 (2014) 214–221, https://doi.org/10.1016/j.conbuildmat.2014.05.063.
[4] M.Á. Sanjuán, E. Estévez, C. Argiz, D. del Barrio, Effect of curing time on granulated blast-furnace slag cement mortars carbonation, Cem. Concr. Compos. 90 (2018) 257–265, https://doi.org/10.1016/j.cemconcomp.2018.04.006.
[5] S. Ahmad, R.A. Assaggaf, M. Maslehuddin, O.S.B. Al-Amoudi, S.K. Adekunle, S. I. Ali, Effects of carbonation pressure and duration on strength evolution of concrete subjected to accelerated carbonation curing, Construct. Build. Mater. 136 (2017) 565–573, https://doi.org/10.1016/j.conbuildmat.2017.01.069.
[6] L. Mo, D.K. Panesar, Accelerated carbonation - a potential approach to sequester CO2 in cement paste containing slag and reactive MgO, Cem. Concr. Compos. 43 (2013) 69–77, https://doi.org/10.1016/j.cemconcomp.2013.07.001.
[7] R.I. Khan, S. Siddique, W. Ashraf, Effects of magnesia in semi-hydraulic and non-hydraulic calcium silicate binders during carbonation curing, Construct. Build. Mater. 338 (2022), 127628, https://doi.org/10.1016/j.conbuildmat.2022.127628.
[8] E. Gruyaert, P. Van Den Heede, N. De Belie, Carbonation of slag concrete: effect of the cement replacement level and curing on the carbonation coefficient - effect of carbonation on the pore structure, Cem. Concr. Compos. 35 (2013) 39–48, https://doi.org/10.1016/j.cemconcomp.2012.08.024.
[9] I. Galan, C. Andrade, P. Mora, M.A. Sanjuan, Sequestration of CO2 by concrete carbonation, Environ. Sci. Technol. 44 (2010) 3181–3186, https://doi.org/10.1021/es903581d.
[10] W. Ashraf, J. Olek, V. Atakan, Carbonation reaction kinetics, CO2 sequestration capacity, and microstructure of hydraulic and non-hydraulic cementitious binders, Sustain. Constr. Mater. Technol. 2016-August (2016).
[11] R.I. Khan, W. Ashraf, J. Olek, Amino acids as performance-controlling additives in carbonation-activated cementitious materials, Cement Concr. Res. 147 (2021) 1–39, https://doi.org/10.1016/j.cemconres.2021.106501.
[12] S.A. Bernal, J.L. Provis, B. Walkley, R. San Nicolas, J.D. Gehman, D.G. Brice, A. R. Kilcullen, P. Duxson, J.S.J. Van Deventer, Gel nanostructure in alkali-activated binders based on slag and fly ash, and effects of accelerated carbonation, Cement Concr. Res. 53 (2013) 127–144, https://doi.org/10.1016/j.cemconres.2013.06.007.
[13] S.A. Bernal, J.L. Provis, D.G. Brice, A. Kilcullen, P. Duxson, J.S.J. Van Deventer, Accelerated carbonation testing of alkali-activated binders significantly underestimates service life: the role of pore solution chemistry, Cement Concr. Res. 42 (2012) 1317–1326, https://doi.org/10.1016/j.cemconres.2012.07.002.
[14] S.A. Bernal, R. San Nicolas, R.J. Myers, R. Mejía De Gutiérrez, F. Puertas, J.S.J. Van Deventer, J.L. Provis, MgO content of slag controls phase evolution and structural changes induced by accelerated carbonation in alkali-activated binders, Cem, Concr. Res. 57 (2014) 33–43, https://doi.org/10.1016/j.cemconres.2013.12.003.
[15] L. Štajner, J. Kontrec, B. Njegić Džakula, N. Maltar-Strmečki, M. Plodinec, D. M. Lyons, D. Kralj, The effect of different amino acids on spontaneous precipitation of calcium carbonate polymorphs, J. Cryst. Growth 486 (2018) 71–81, https://doi.org/10.1016/j.jcrysgro.2018.01.023.
[16] M.G. Ma, S. Liu, L.H. Fu, Calcium carbonate and cellulose/calcium carbonate composites: synthesis, characterization, and biomedical applications, Mater. Sci. Forum 875 (2016) 24–44. https://doi.org/10.4028/www.scientific.net/MSF.875.24.
[17] S. Kim, C.B. Park, Dopamine-induced mineralization of calcium carbonate vaterite microspheres, Langmuir 26 (2010) 14730–14736, https://doi.org/10.1021/la1027509.
[18] Y. Fang, J. Wang, X. Qian, L. Wang, G. Lin, Z. Liu, Bio-inspired functionalization of very fine aggregates for better performance of cementitious materials, Construct. Build. Mater. 241 (2020), 118104, https://doi.org/10.1016/j.conbuildmat.2020.118104.
[19] M. Wu, T. Wang, Y. Wang, H. Wang, Ultrafast bone-like apatite formation on bioactive tricalcium silicate cement using mussel-inspired polydopamine, Ceram. Int. 45 (2019) 3033–3043, https://doi.org/10.1016/j.ceramint.2018.10.149.
[20] S. Kim, J.W. Ko, C.B. Park, Bio-inspired mineralization of CO2 gas to hollow CaCO 3 microspheres and bone hydroxyapatite/polymer composites, J. Mater. Chem. 21 (2011) 11070–11073, https://doi.org/10.1039/c1jm12616d.
[21] S.S. Wang, A.W. Xu, Amorphous calcium carbonate stabilized by a flexible biomimetic polymer inspired by marine mussels, Cryst. Growth Des. 13 (2013) 1937–1942, https://doi.org/10.1021/cg301759t.
[22] Z. Liu, S. Qu, X. Zheng, X. Xiong, R. Fu, K. Tang, Z. Zhong, J. Weng, Effect of polydopamine on the biomimetic mineralization of mussel-inspired calcium phosphate cement in vitro, Mater. Sci. Eng. C 44 (2014) 44–51, https://doi.org/10.1016/j.msec.2014.07.063.
[23] Z. Li, B. Peng, Z. Deng, Biomimetic synthesis of calcium carbonate films on bioinspired polydopamine matrices, J. Coating Technol. Res. 14 (2017) 1095–1105, https://doi.org/10.1007/s11998-016-9898-x.
[24] S.J. Peters, T.S. Rushing, E.N. Landis, T.K. Cummins, Nanocellulose and microcellulose fibers for concrete, Transport. Res. Rec. (2010) 25–28, https://doi.org/10.3141/2142-04.
[25] O. Onuaguluchi, N. Banthia, Plant-based natural fibre reinforced cement composites: a review, Cem. Concr. Compos. 68 (2016), https://doi.org/10.1016/j.cemconcomp.2016.02.014.
[26] Y. Guo, F. Wang, J. Zhang, L. Yang, Biomimetic Synthesis of Calcium Carbonate with Different Morphologies under the Direction of Different Amino Acids, 2012, pp. 2407–2415, https://doi.org/10.1007/s11164-012-0767-7.
[27] P. Kumaresan, Thermal , dielectric studies on pure and amino acid (L -glutamic acid, L -histidine, L -valine) doped, KDP single crystals 30 (2008) 1361–1368, https://doi.org/10.1016/j.optmat.2007.07.002.
[28] Y.Y. Kim, J.D. Carloni, B. Demarchi, D. Sparks, D.G. Reid, M.E. Kunitake, C. C. Tang, M.J. Duer, C.L. Freeman, B. Pokroy, K. Penkman, J.H. Harding, L. A. Estroff, S.P. Baker, F.C. Meldrum, Tuning hardness in calcite by incorporation of amino acids, Nat. Mater. 15 (2016) 903–910, https://doi.org/10.1038/nmat4631.
[29] W.B. Tsai, W.T. Chen, H.W. Chien, W.H. Kuo, M.J. Wang, Poly(dopamine) coating of scaffolds for articular cartilage tissue engineering, Acta Biomater. 7 (2011) 4187–4194, https://doi.org/10.1016/j.actbio.2011.07.024.
[30] Q. Ye, F. Zhou, W. Liu, Bioinspired catecholic chemistry for surface modification, Chem. Soc. Rev. 40 (2011) 4244–4258, https://doi.org/10.1039/c1cs15026j.
[31] B.P. Lee, P.B. Messersmith, J.N. Israelachvili, J.H. Waite, Mussel-inspired adhesives and coatings, Annu. Rev. Mater. Res. 41 (2011) 99–132, https://doi.org/10.1146/annurev-matsci-062910-100429.
[32] P. Soroushian, J.P. Won, M. Hassan, Durability characteristics of CO 2-cured cellulose fiber reinforced cement composites, Construct. Build. Mater. 34 (2012) 44–53, https://doi.org/10.1016/j.conbuildmat.2012.02.016.
[33] N. Saleh, P. Ziehl, F. Matta, N. Aich, N. Zohhadi, I.A. Khan, POLYMERICADDITIVE for strength, deformability. And toughness enhancement of CEMENTITIOUS MATERIALS and composites, U. S. Jpn. Outlook 8 (2014), 907,050 B2, https://patentimages.storage.googleapis.com/9e/9a/7d/d54373c24662be/US8907050.pdf.
[34] T. Gebregiorgis, M. Vaccari, S. Prasad, E.D. Van Hullebusch, S. Rtimi, Preparation and Applications of Chitosan and Cellulose Composite Materials, 2022, p. 301, https://doi.org/10.1016/j.jenvman.2021.113850.
[35] M. Alavi, M. Rai, Recent progress in nanoformulations of silver nanoparticles with cellulose, chitosan, and alginic acid biopolymers for antibacterial applications, Appl. Microbiol. Biotechnol. 103 (2019) 8669–8676, https://doi.org/10.1007/s00253-019-10126-4.
[36] C. Son, S. Chung, J. Lee, S. Kim, Isolation and cultivation characteristics of Acetobacter xylinum KJ-1 producing bacterial cellulose in shaking cultures, J. Microbiol. Biotechnol. 12 (2002).
[37] D. Mazlan, M.F. Md Din, C. Tokoro, I.S. Ibrahim, Cellulose nanocrystals addition effects on cement mortar matrix properties, Int. J. Adv. Mech. Civ. Eng. 3 (2016).
[38] M.R. Hossen, N. Dadoo, D.G. Holomakoff, A. Co, W.M. Gramlich, M.D. Mason, Wet stable and mechanically robust cellulose nanofibrils (CNF) based hydrogel, Polymer 151 (2018), https://doi.org/10.1016/j.polymer.2018.07.016.

[39] R.J. Moon, A. Martini, J. Nairn, J. Simonsen, J. Youngblood, Cellulose nanomaterials review: structure, properties and nanocomposites, Chem. Soc. Rev. 40 (2011), https://doi.org/10.1039/c0cs00108b.
[40] L. Zhai, H.C. Kim, J.W. Kim, J. Kang, J. Kim, Elastic moduli of cellulose nanofibers isolated from various cellulose resources by using aqueous counter collision, Cellulose 25 (2018), https://doi.org/10.1007/s10570-018-1836-x.
[41] Q. Tarrés, S. Boufi, P. Mutjé, M. Delgado-Aguilar, Enzymatically hydrolyzed and TEMPO-oxidized cellulose nanofibers for the production of nanopapers: morphological, optical, thermal and mechanical properties, Cellulose 24 (2017), https://doi.org/10.1007/s10570-017-1394-7.
[42] B. Cantaert, D. Kuo, S. Matsumura, T. Nishimura, T. Sakamoto, T. Kato, Use of amorphous calcium carbonate for the design of new materials, Chempluschem 82 (2017) 107–120, https://doi.org/10.1002/cplu.201600457.
[43] K.S. Kamasamudram, W. Ashraf, E.N. Landis, R.I. Khan, Effects of ligno– and delignified– cellulose nanofibrils on the performance of cement-based materials, J. Mater. Res. Technol. 13 (2021) 321–335, https://doi.org/10.1016/j.jmrt.2021.04.090.
[44] M.A. Akhlaghi, R. Bagherpour, H. Kalhori, Application of bacterial nanocellulose fibers as reinforcement in cement composites, Construct. Build. Mater. 241 (2020), 118061, https://doi.org/10.1016/j.conbuildmat.2020.118061.
[45] K.S. Kamasamudram, W. Ashraf, E.N. Landis, Cellulose nanofibrils with and without nanosilica for the performance enhancement of Portland cement systems, Construct. Build. Mater. 285 (2021), https://doi.org/10.1016/j.conbuildmat.2020.121547.
[46] T.F.R. Claramunt J, M. Ardanuy, R. Arevalo, F. Pares, Mechanical performance of ductile cement mortar composites reinforced with nanofibrillated cellulose, Strain Hardening Cem, Compos (2011) 131–138.
[47] O.A. Hisseine, A.F. Omran, A. Tagnit-Hamou, Influence of cellulose filaments on cement paste and concrete, J. Mater. Civ. Eng. 30 (2018) 1–14, https://doi.org/10.1061/(ASCE)MT.1943-5533.0002287.
[48] ASTM, C157/C157M-08, standard test method for length change of hardened hydraulic-cement mortar and concrete, ASTM Int. (2008) 1–7, https://doi.org/10.1520/C0157, 08.
[49] I. Odler, The BET-specific surface area of hydrated Portland cement and related materials, Cement Concr. Res. 33 (2003) 2049–2056, https://doi.org/10.1016/S0008-8846(03)00225-4.
[50] S. Brunauer, P.H. Emmett, E. Teller, Adsorption of gases in multimolecular layers, J. Am. Chem. Soc. 60 (1938) 309–319.
[51] P.P.Barrett Elliott, Leslei G. Joyner, Halenda, The Determination of Pore Volume and Area Distributions in Porous Substances. I. Computations from Nitrogen Isotherms, 1951.
[52] W. Ashraf, J. Olek, Elucidating the accelerated carbonation products of calcium silicates using multi-technique approach, J. CO2 Util. 23 (2018) 61–74, https://doi.org/10.1016/j.jcou.2017.11.003.
[53] D.K. Panesar, J. Francis, Influence of limestone and slag on the pore structure of cement paste based on mercury intrusion porosimetry and water vapour sorption measurements, Construct. Build. Mater. 52 (2014) 52–58, https://doi.org/10.1016/j.conbuildmat.2013.11.022.
[54] M.I. Haque, W. Ashraf, R.I. Khan, S. Shah, A comparative investigation on the effects of nanocellulose from bacteria and plant-based sources for cementitious composites, Cem. Concr. Compos. 125 (2022), 104316, https://doi.org/10.1016/j.cemconcomp.2021.104316.
[55] W. Ashraf, J. Olek, N. Tian, Multiscale characterization of carbonated wollastonite paste and application of homogenization schemes to predict its effective elastic modulus, Cem. Concr. Compos. 72 (2016) 284–298, https://doi.org/10.1016/j.cemconcomp.2016.05.023.
[56] F. Ulm, M. Vandamme, C. Bobko, J.A. Ortega, Statistical indentation techniques for hydrated nanocomposites: concrete, Bone, and Shale (2007) 2692, https://doi.org/10.1111/j.1551-2916.2007.02012.x.
[57] G. Constantinides, K.S. Ravi Chandran, F.J. Ulm, K.J. Van Vliet, Grid indentation analysis of composite microstructure and mechanics: principles and validation, Mater. Sci. Eng. 430 (2006) 189–202, https://doi.org/10.1016/j.msea.2006.05.125.
[58] Y. Cao, P. Zavaterri, J. Youngblood, R. Moon, J. Weiss, The influence of cellulose nanocrystal additions on the performance of cement paste, Cem. Concr. Compos. 56 (2015) 73–83, https://doi.org/10.1016/j.cemconcomp.2014.11.008.
[59] H.H. Kolour, M. Ahmed, E. Alyaseen, E.N. Landis, An investigation on the effects of cellulose nanofibrils on the performance of cement paste and concrete, Adv. Civ. Eng. Mater. 7 (2018), https://doi.org/10.1520/ACEM20180048.
[60] M.S. Eisa, M.E. Basiouny, E.A. Fahmy, Effect of metakaolin-based geopolymer concrete on the length of rigid pavement slabs, Innov. Infrastruct. Solut. 6 (2021) 1–9, https://doi.org/10.1007/s41062-021-00465-5.
[61] M. Hsie, C. Tu, P.S. Song, Mechanical properties of polypropylene hybrid fiber-reinforced concrete, Mater. Sci. Eng. 494 (2008) 153–157, https://doi.org/10.1016/j.msea.2008.05.037.
[62] N.S. Folliard, J. Kevin, Berke, Properties of high-performance concrete containing shrinkage-reducing admixture, Angew. Chem. Int. Ed. 6 (11) (1967) 951–952, https://doi.org/10.1016/S0008-8846(97)00135-X, 1357–1364.
[63] R.I. Khan, W. Ashraf, Effects of ground wollastonite on cement hydration kinetics and strength development, Construct. Build. Mater. 218 (2019) 150–161, https://doi.org/10.1016/j.conbuildmat.2019.05.061.
[64] I.M. Weiss, C. Muth, R. Drumm, H.O.K. Kirchner, Thermal decomposition of the amino acids glycine, cysteine, aspartic acid, asparagine, glutamic acid, glutamine, arginine and histidine Ingrid M. Weiss*, Christina Muth, Robert Drumm & Helmut O.K. Kirchner, (2017) 1–23.
[65] W. Ashraf, J. Olek, Elucidating the accelerated carbonation products of calcium silicates using multi-technique approach, J. CO2 Util. 23 (2018), https://doi.org/10.1016/j.jcou.2017.11.003.
[66] J. Ihli, W.C. Wong, E.H. Noel, Y.Y. Kim, A.N. Kulak, H.K. Christenson, M.J. Duer, F. C. Meldrum, Dehydration and crystallization of amorphous calcium carbonate in solution and in air, Nat. Commun. 5 (2014) 1–10, https://doi.org/10.1038/ncomms4169.
[67] L. Jiao, M. Su, L. Chen, Y. Wang, H. Zhu, H. Dai, Natural cellulose nanofibers as sustainable enhancers in construction cement, PLoS One 11 (2016), https://doi.org/10.1371/journal.pone.0168422.
[68] W. Ashraf, J. Olek, Carbonation behavior of hydraulic and non-hydraulic calcium silicates: potential of utilizing low-lime calcium silicates in cement-based materials, J. Mater. Sci. 51 (2016) 6173–6191, https://doi.org/10.1007/s10853-016-9909-4.
[69] P. Yu, R.J. Kirkpatrick, B. Poe, P.F. McMillan, X. Cong, Structure of Calcium Silicate Hydrate, Mid-, and Far-Infrared Spectroscopy, 2004, https://doi.org/10.1111/j.1151-2916.1999.tb01826.x.
[70] A. Puertas, F. Fernandez-Jimenez, Mineralogical and microstructural characterisation of alkali-activated fly ash/slag pastes, Environ. - MDPI. 4 (2017) 1–14, https://doi.org/10.3390/environments4030044.
[71] K. Kupwade-Patil, S.D. Palkovic, A. Bumajdad, C. Soriano, O. Büyüköztürk, Use of silica fume and natural volcanic ash as a replacement to Portland cement: micro and pore structural investigation using NMR, XRD, FTIR and X-ray microtomography, Construct. Build. Mater. 158 (2018) 574–590, https://doi.org/10.1016/j.conbuildmat.2017.09.165.
[72] N. Li, N. Farzadnia, C. Shi, Microstructural changes in alkali-activated slag mortars induced by accelerated carbonation, Cem, Concr. Res. 100 (2017) 214–226, https://doi.org/10.1016/j.cemconres.2017.07.008.
[73] Z. Shi, C. Shi, S. Wan, N. Li, Z. Zhang, Effect of alkali dosage and silicate modulus on carbonation of alkali-activated slag mortars, Cement Concr. Res. 113 (2018) 55–64, https://doi.org/10.1016/j.cemconres.2018.07.005.
[74] M. Sato, S. Matsuda, Structure of vaterite and infrared spectra, Zeitschrift Fur Krist. - New Cryst. Struct. 129 (1969) 405–410, https://doi.org/10.1524/zkri.1969.129.5-6.405.
[75] L. Addadi, S. Raz, S. Weiner, Taking advantage of disorder: amorphous calcium carbonate and its roles in biomineralization, Adv. Mater. 15 (2003) 959–970, https://doi.org/10.1002/adma.200300381.
[76] S. Kim, C.B. Park, Mussel-inspired transformation of CaCO3 to bone minerals, Biomaterials 31 (2010) 6628–6634, https://doi.org/10.1016/j.biomaterials.2010.05.004.
[77] M. Saharay, A.O. Yazaydin, R.J. Kirkpatrick, Dehydration-induced amorphous phases of calcium carbonate, J. Phys. Chem. B 117 (2013) 3328–3336, https://doi.org/10.1021/jp308353t.
[78] image. sc, Image processing and analysis in Java (ImageJ), 2021 n.d. https://imagej.nih.gov/ij/download.html.
[79] V. Baroghel-Bouny, Water vapour sorption experiments on hardened cementitious materials. Part I: essential tool for analysis of hygral behaviour and its relation to pore structure, Cement Concr. Res. 37 (2007) 414–437, https://doi.org/10.1016/j.cemconres.2006.11.019.
[80] A. Rodriguez-navarro, C. Jimenez-lopez, A. Checa, J.M.G.- Ruiz, Nanocrystalline structures in calcium carbonate biominerals, J. Nanophotonics (2008), https://doi.org/10.1117/1.3062826.
[81] W. Ashraf, J. Olek, J. Jain, Microscopic features of non-hydraulic calcium silicate cement paste and mortar, Cement Concr. Res. 100 (2017) 361–372, https://doi.org/10.1016/j.cemconres.2017.07.001.
[82] W. Ashraf, J. Olek, Carbonation activated binders from pure calcium silicates: reaction kinetics and performance controlling factors, Cem. Concr. Compos. 93 (2018) 85–98, https://doi.org/10.1016/j.cemconcomp.2018.07.004.
[83] M. Miller, C. Bobko, M. Vandamme, F. Ulm, Surface roughness criteria for cement paste nanoindentation, Cement Concr. Res. 38 (2008) 467–476, https://doi.org/10.1016/j.cemconres.2007.11.014.
[84] Y. Li, Y. Liu, R. Wang, Evaluation of the elastic modulus of concrete based on indentation test and multi-scale homogenization method, J. Build. Eng. 43 (2021), 102758, https://doi.org/10.1016/j.jobe.2021.102758.
[85] N.K. Dhami, A. Mukherjee, M.S. Reddy, Micrographical, mineralogical and nano-mechanical characterisation of microbial carbonates from urease and carbonic anhydrase producing bacteria, Ecol. Eng. 94 (2016) 443–454, https://doi.org/10.1016/j.ecoleng.2016.06.013.
[86] B. Lothenbach, A. Nonat, Calcium silicate hydrates: solid and liquid phase composition, Cement Concr. Res. 78 (2015) 57–70, https://doi.org/10.1016/j.cemconres.2015.03.019.
[87] B.K. Ahn, S. Das, R. Linstadt, Y. Kaufman, N.R. Martinez-Rodriguez, R. Mirshafian, E. Kesselman, Y. Talmon, B.H. Lipshutz, J.N. Israelachvili, J.H. Waite, High-performance mussel-inspired adhesives of reduced complexity, Nat. Commun. 6 (2015) 4–10, https://doi.org/10.1038/ncomms9663.